

HSTPROMO Internal Proper Motion Kinematics of Dwarf Spheroidal Galaxies: II. Velocity Anisotropy and Dark Matter Cusp Slope of Sculptor

EDUARDO VITRAL ^{1,2,*} ROELAND P. VAN DER MAREL ^{2,3} SANGMO TONY SOHN ^{2,4} JORGE PEÑARRUBIA,^{1,5}
EKTA PATEL ^{6,7,†} LAURA L. WATKINS ⁸ MATTIA LIBRALATO ⁹ KEVIN A. MCKINNON ¹⁰ ANDREA BELLINI ² AND
PAUL BENNET ²

¹*Institute for Astronomy, University of Edinburgh, Royal Observatory, Blackford Hill, Edinburgh EH9 3HJ, UK*

²*Space Telescope Science Institute, 3700 San Martin Drive, Baltimore, MD 21218, USA*

³*Center for Astrophysical Sciences, The William H. Miller III Department of Physics & Astronomy, Johns Hopkins University, Baltimore, MD 21218, USA*

⁴*Dept. of Astronomy & Space Science, Kyung Hee University, Gyeonggi-do 17104, Republic of Korea*

⁵*Centre for Statistics, University of Edinburgh, School of Mathematics, Edinburgh EH9 3FD, UK*

⁶*Department of Physics and Astronomy, University of Utah, 115 South 1400 East, Salt Lake City, Utah 84112, USA*

⁷*Department of Astrophysics and Planetary Sciences, Villanova University, 800 E. Lancaster Ave, Villanova, PA 19085, USA*

⁸*AURA for the European Space Agency (ESA), Space Telescope Science Institute, 3700 San Martin Drive, Baltimore, MD 21218, USA*

⁹*INAF - Osservatorio Astronomico di Padova, Vicolo dell'Osservatorio 5, Padova I-35122, Italy*

¹⁰*David A. Dunlap Department of Astronomy & Astrophysics, University of Toronto, 50 St. George Street, Toronto, ON M5S 3H4, Canada*

ABSTRACT

We analyze three epochs of *HST* imaging over 20 years for the Sculptor dwarf spheroidal galaxy, measuring precise proper motions for 119 stars and combining them with 1,760 existing line-of-sight velocities. This catalog yields the first radially-resolved 3D velocity dispersion profiles for Sculptor. We confirm mild oblate rotation, with major-axis velocities reaching $\sim 2 \text{ km s}^{-1}$ beyond $20''$. Using a methodology similar to that in the first paper in this series, we solve the Jeans equations in oblate axisymmetric geometry to infer the galaxy's mass profile. Our modeling reveals a significant degeneracy due to the unknown galaxy inclination, which is overlooked under spherical symmetry assumptions. This degeneracy allows acceptable fits across a range of dark matter profiles, from cuspy to cored. While we do not directly constrain the inclination with our Jeans models, higher-order line-of-sight velocity moments provide useful additional constraints: comparisons with SCALEFREE models from de Bruijne et al. (1996) favor highly flattened (more face-on) configurations. Adopting an inclination well consistent with these comparisons ($i = 57^\circ$), we find, alongside radial velocity anisotropy, a dark matter density slope of $\Gamma_{\text{dark}} = 0.29^{+0.31}_{-0.41}$ within the radial extent of the 3D velocity data, ruling out a cusp with $\Gamma_{\text{dark}} \leq -1$ at 99.8% confidence. This confidence increases for lower inclinations and decreases drastically for nearly edge-on configurations. The results qualitatively agree with Λ CDM, SIDM, and Fuzzy DM scenarios that predict core formation, while our specific measurements provide quantitative constraints on the prescriptions of feedback, cross sections, or particle masses required by these models, respectively.

Keywords: dark matter — galaxies: dwarf — galaxies: structure — methods: data analysis — proper motions — stars: kinematics and dynamics

1. INTRODUCTION

The nature of dark matter (DM) remains one of the most profound open questions in modern astrophysics, with far-reaching implications for both cosmology and our understanding of galaxy formation

Corresponding author: Eduardo Vitral
eduardo.vital@roe.ac.uk

* Royal Society Newton International Fellow

† NASA Hubble Fellow

(Bertone, Hooper, & Silk 2005; Silk & Mamon 2012). Among the environments in which DM can be studied, dwarf spheroidal galaxies (dSphs) stand out as particularly valuable laboratories (Strigari 2013; Collins & Read 2022). These small, faint systems are among the most DM-dominated objects known (Pryor & Kormendy 1990), making them highly sensitive to the properties of DM on small scales (Bullock & Boylan-Kolchin 2017). Their relatively simple stellar populations and quiescent evolutionary histories (Tolstoy, Hill, & Tosi 2009; Savino et al. 2025) also provide a cleaner view of internal dynamical processes than the more complex environments found in larger galaxies (Grebel 2009).

Accurately inferring the internal kinematics of dSphs remains a long-standing challenge. Analyses based solely on line-of-sight (LOS) velocities¹ are fundamentally limited by the well-known degeneracy between the mass distribution and the orbital anisotropy of the stellar component (Binney & Mamon 1982). This degeneracy hampers efforts to robustly distinguish between different DM density profiles, complicating tests of predictions from Λ Cold Dark Matter (Λ CDM) and alternative cosmological models (Bolchini 2021). Overcoming this limitation typically requires either modeling techniques that incorporate higher-order velocity moments (Chanamé, Kleyna, & van der Marel 2008; Read & Steger 2017) – which remain difficult to constrain with current LOS data – or the inclusion of transverse stellar motions in the plane of the sky (van der Marel & Anderson 2010). The latter has historically been inaccessible for galaxies beyond the Milky Way (Gaia Collaboration et al. 2018), owing to the simultaneous need for long time baselines (typically $\gtrsim 10$ yrs) and high-precision astrometry to reach sufficiently small uncertainties.

The advent of space-based astrometry has now opened new avenues for addressing this limitation. Transverse velocity measurements, or proper motions (PMs), can be obtained with high precision and, when combined with LOS velocities, enable the reconstruction of full three-dimensional velocity vectors for stars in nearby dSphs (Massari et al. 2017, 2020; del Pino et al. 2022; Libralato et al. 2023; Vitral et al. 2024; McKinnon et al. 2024). These additional kinematic dimensions significantly enhance the constraining power of dynamical models and allow for a more complete and direct view of a system’s internal dynamics than can be obtained from LOS velocities alone (Read et al. 2021).

¹ Motions toward or away from the observer, measured through spectroscopic data typically obtained from ground-based observatories.

In a series of papers beginning with Vitral et al. (2024, hereafter Paper I), we aim to construct comprehensive PM catalogs for nearby dSphs and use them, alongside LOS velocities, to build detailed dynamical models of these systems. By systematically applying these techniques, we seek to refine our understanding of their underlying DM distributions and evaluate the influence of baryonic processes in shaping both their internal kinematics and DM density profiles. In the first paper of this series, we analyzed the Draco dSph and found that its internal dynamics are consistent with a cuspy DM profile, as predicted by DM-only Λ CDM simulations (Navarro, Frenk, & White 1997). In this second study, we turn our attention to the Sculptor dSph (also known as PGC3589, MCG-06-03-015, or ESO351-30), a well-studied system (Battaglia et al. 2008; Walker & Peñarrubia 2011; Massari et al. 2017; Arroyo-Polonio et al. 2025) which, until now, lacked a large and homogeneous PM dataset with uncertainties smaller than its intrinsic velocity dispersion. Such precision is essential to mitigate the impact of measurement errors and systematic biases in dynamical mass estimates (Watkins et al. 2013; Vitral et al. 2022), as discussed in Paper I. Among Sculptor’s notable features is its higher stellar mass relative to Draco (Martin et al. 2008; de Boer et al. 2012), placing the two galaxies on opposite sides of the threshold where baryonic processes are thought to flatten DM cusps (Fitts et al. 2017), despite their broadly similar structural properties (Muñoz et al. 2018).

With this background in mind, the remainder of the paper is structured as follows. Section 2 outlines the general properties of Sculptor relevant to our modeling and describes the kinematic datasets used throughout the study. Section 3 details the modeling techniques employed to analyze the galaxy. Sections 4 and 5 present our main results and assess their robustness, respectively. Section 6 discusses the implications of our findings for mass modeling and broader cosmological questions. Finally, Section 7 summarizes our key conclusions.

2. SCULPTOR DATA AND GENERAL CHARACTERISTICS

2.1. Structural Parameters

We begin by defining and presenting the structural parameters used as input throughout this work – namely, the shape of the stellar mass density profile, characterized by the total stellar mass, its scale radius, and the position of the galaxy’s center of mass (hereafter simply center). The position of Sculptor’s center, as listed in

Table 1. Overview of Sculptor structural parameters.

Reference	Data	α_0	δ_0	θ	ϵ	R_h
(1)	(2)	(3)	(4)	(5)	(6)	(7)
This work	Gaia EDR3	$15^\circ 02328 \pm 8'' 2$	$-33^\circ 71504 \pm 4'' 8$	$95^\circ 4 \pm 1^\circ 6$	0.272 ± 0.013	$11' 12 \pm 0' 17$
Muñoz et al. (2018)	MegaCam	$15^\circ 01830 \pm 0'' 3$	$-33^\circ 71860 \pm 2'' 6$	$92^\circ 0 \pm 1^\circ 0$	0.330 ± 0.010	$11' 17 \pm 0' 05$

NOTES – Columns are **(1)** Reference where the values are reported; **(2)** data source of respective estimates (columns 3–7); **(3)** right ascension of Sculptor center; **(4)** declination of Sculptor center; **(5)** Major axis projected angle in the sky, from North to East; **(6)** projected ellipticity in the sky, defined as $1 - b/a$, with a and b the major and minor axes of the projected ellipse, respectively; **(7)** 2D half-number radius of a Plummer model fit (i.e. the major axis of the ellipse that contains half the stellar count).

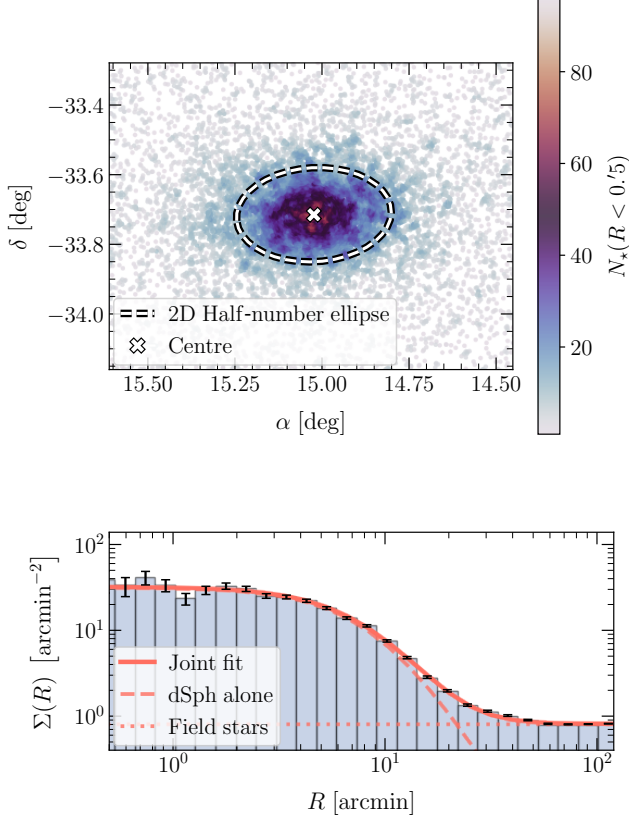


Figure 1. *Geometry and density:* The **top** panel presents a sky view of Sculptor, with *Gaia* EDR3 measurements scattered and color-coded by the number of neighbors within a 0.5 projected radius. The 2D half-number ellipse and the center from our fits are shown as a white dashed line and a white cross, respectively. The **lower** panel shows the observed surface number density of stars within an annulus at radius R – the projected distance from the center of Sculptor – in blue, along with the corresponding model fit, decomposed into its individual components: the dSph alone in dashed red, the interlopers in dotted red, and their sum in solid red. The figure highlights a satisfactory fit of Sculptor’s structural parameters to the *Gaia* EDR3 data.

the [McConnachie \(2012\)](#) catalog and the Local Volume Database ([Pace 2024](#)), originates from its initial discovery by [Shapley \(1938\)](#). Recently, [Muñoz et al. \(2018\)](#) refined Sculptor’s center and structural parameters using Canada France Hawaii Telescope’s MegaCam imaging. Their analysis provided more reliable estimates based on improved stellar measurements. In this study, we adopt a similar fitting methodology to [Muñoz et al. \(2018\)](#), also employed in Paper I (see the latter’s section 2.1.1 and eq. A2). Specifically, we fit an axisymmetric [Plummer \(1911\)](#) model to *Gaia* EDR3 star counts, incorporating a constant-density interloper background to derive Sculptor’s structural parameters and central position.

Our goodness-of-fit results are summarized in Figure 1, which compares the *Gaia* EDR3 data with our best-fitting structural model. The top panel shows a centered sky view of Sculptor, where individual *Gaia* sources are color-coded by the local stellar count within 0.5 . The fitted center (white cross) lies close to the observed density maximum, and the model’s 2D half-number ellipse (white dashed line) traces the projected stellar distribution well. The lower panel presents the azimuthally averaged surface number density as a function of projected radius R . The observed profile (blue) is well matched by the sum (solid red) of two components: the dSph itself (dashed red) and a uniform interloper background (dotted red). The good agreement in both the spatial distribution and radial profile indicates that our model captures Sculptor’s sky orientation, central position, and overall surface density structure. The parameters derived from this fit are presented in Table 1, alongside those reported by [Muñoz et al. \(2018\)](#).

The overall shape of Sculptor – quantified here by its position angle θ , ellipticity ϵ , and projected half-number radius R_h – agrees closely with the results of [Muñoz et al. \(2018\)](#). In our convention, $\epsilon \equiv 1 - b/a$, where a and b are the major and minor axes of the best-fitting photometric ellipse, and θ is the position angle of the major axis measured from north toward east. The half-number radius R_h corresponds to the major axis length

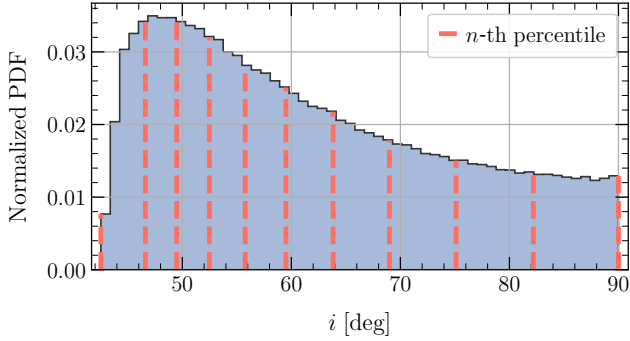


Figure 2. *Inclinations:* Probability distribution function of inclinations for Sculptor, computed using the formalism described in Paper I (section 2.1.3). The dashed red lines represent the n -th percentiles of the distribution, where n ranges from zero to a hundred, in intervals of ten.

of the ellipse enclosing half the stars in a Plummer model fit. Our fitted center lies in between the [Shapley \(1938\)](#) and [Muñoz et al. \(2018\)](#) values, with respective distances of $52''.5$ and $19''.7$ from each.

The flattening of Sculptor closely resembles that of Draco, resulting in a probability distribution function (PDF) of possible inclinations that follows a similarly shaped curve. This PDF is calculated using the formalism from Paper I (see section 2.1.3), which is based on the statistical distribution of elliptical galaxy shapes inferred by [Lambas et al. \(1992\)](#). The resulting distribution is shown in Figure 2. The [16, 50, 84] percentiles for the inclination and 3D flattening distributions are $[48^\circ 34', 59^\circ 50', 77^\circ 82']$ and $[0.38, 0.60, 0.71]$, respectively.

Finally, we consider Sculptor’s stellar mass as estimated by [de Boer et al. \(2012\)](#) based on its star formation history and color-magnitude diagram (CMD). They report a stellar mass of $7.8 \times 10^6 M_\odot$ within a $1''.0$ elliptical radius.² Extrapolating this measurement to infinity, assuming an axisymmetric Plummer density profile, yields a total stellar mass of $8.08 \times 10^6 M_\odot$, which is adopted throughout this work.³

2.2. Line-of-Sight Velocities

Similarly to Paper I, we use the spectroscopic catalog from [Walker et al. \(2023\)](#) to obtain LOS velocities

² Their definition of an elliptical radius, clarified through private communication with T. J. L. de Boer, involves projecting the (α, δ) data onto (x, y) Cartesian coordinates, rotating them by Sculptor’s position angle, and dividing the y coordinate by $(1-\epsilon)$. The elliptical radius is then calculated as $\sqrt{x'^2 + y'^2}$, where x' and y' are the rotated and scaled Cartesian coordinates.

³ For context, this value relates to a DM halo mass of $M_{\text{dark}} = 4.85 \times 10^9 M_\odot$ in Λ CDM cosmology, using the relation for low-mass dwarfs from [Read et al. \(2017\)](#).

for our mass modeling. Following the same data cleaning procedures detailed in Paper I (see section 2.2.1), we identify 1151 Sculptor members from this catalog. To augment this dataset, we incorporate the recently published spectroscopic measurements by [Tolstoy et al. \(2023\)](#), which are derived from *Gaia* and VLT/FLAMES observations. We clean the [Tolstoy et al. \(2023\)](#) catalog following their recommended criteria: setting the z coefficient⁴ ≤ 14.2 , enforcing $S/N > 20$, and selecting only stars classified as members in their analysis. This procedure yields an additional 1123 LOS velocities. For both catalogs, we apply corrections for perspective motions using the formalism from [van der Marel et al. \(2002, eq. 13\)](#).

To leverage the strengths and coverage of both datasets, we merge them using the following approach:

1. We first identify common stars in the two catalogs by performing a symmetric sky match with a maximum separation of $1''.0$. This matched subset serves as the basis for comparison. For each catalog, we compute zero-points for LOS velocities using the following steps:
 - (a) Compute the weighted mean of the LOS velocities for the matched stars in each catalog.
 - (b) For each catalog, calculate the distribution of velocity offsets as the difference between the LOS velocities of individual stars and the weighted mean of the matched subset.
 - (c) Derive the zero-point correction for each catalog by taking the weighted mean of these velocity offset distributions.
2. The computed zero-point corrections are applied to the LOS velocities in each catalog,⁵ ensuring consistency between the datasets.
3. Finally, we construct the merged catalog by treating matched stars as single entries. For these matched stars, already corrected for the zero-point, we calculate a common LOS velocity and its associated uncertainty using the weighted mean

⁴ [Tolstoy et al. \(2023\)](#) define z as a membership score based on *Gaia*’s PMs and parallaxes.

⁵ This common treatment is done since we lack an independent means of determining which catalog’s zero-point is intrinsically more accurate. Instead, we align both to a common scale using uncertainty-weighted averages, which incorporate each catalog’s reported precision. The resulting shifts are negligible compared to the velocity scales of interest in this work (e.g., $\sim 2 \text{ km s}^{-1}$ rotation and $\sim 10 \text{ km s}^{-1}$ dispersion): $0.03 \pm 0.01 \text{ km s}^{-1}$ for the [Walker et al. \(2023\)](#) data and $-0.32 \pm 0.03 \text{ km s}^{-1}$ for the [Tolstoy et al. \(2023\)](#) data.

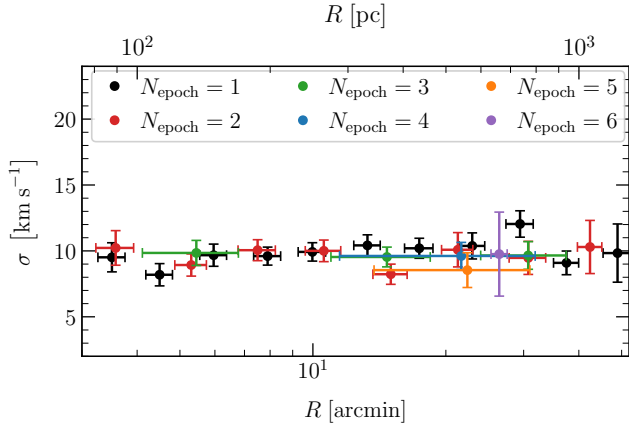


Figure 3. *Impact of unresolved binaries:* We compare multi-epoch velocity dispersion profiles as a function of projected radii for groups of LOS data categorized by the number of measured epochs. Due to the limited number of stars with multi-epoch observations, the corresponding profiles have fewer radial bins. The excellent agreement within $1\text{-}\sigma$ across all N_{epoch} groups, combined with the fact that the σ_{LOS} profiles for higher N_{epoch} are not significantly smaller than those for the $N_{\text{epoch}} = 1$ subset, provides strong confidence that unresolved binaries do not influence our mass estimates beyond the statistical uncertainties.

of their individual measurements.⁶ Stars without matches are retained in the catalog unchanged, aside from the applied zero-point adjustment.

The resulting combined catalog contains 1,760 Sculptor members with LOS velocity uncertainties smaller than the galaxy’s intrinsic velocity dispersion.⁷ This merged dataset represents the most comprehensive spectroscopic catalog assembled for any dwarf galaxy to date.

2.2.1. Binaries

In recent years, unresolved binaries in stellar systems have garnered increased attention due to their potential role in inflating velocity dispersion profiles, which can result in overestimating the mass budget (e.g., [Rastello et al. 2020](#); [Pianta et al. 2022](#)). However, our previous analyses of Draco showed no significant impact from binaries, despite its high binary fraction ([Spencer et al. 2018](#)). This raises the question of how such inflation patterns might depend on various data characteristics, such as the velocity dispersion and the number of measured

⁶ We do not simply adopt the entry from the catalog with the smallest nominal error, as uncertainty-weighted averaging makes optimal use of both measurements and yields the most precise estimate.

⁷ This threshold is critical for robust mass modeling, as highlighted in Paper I and other studies (e.g., [Vitril et al. 2022, 2023a](#)).

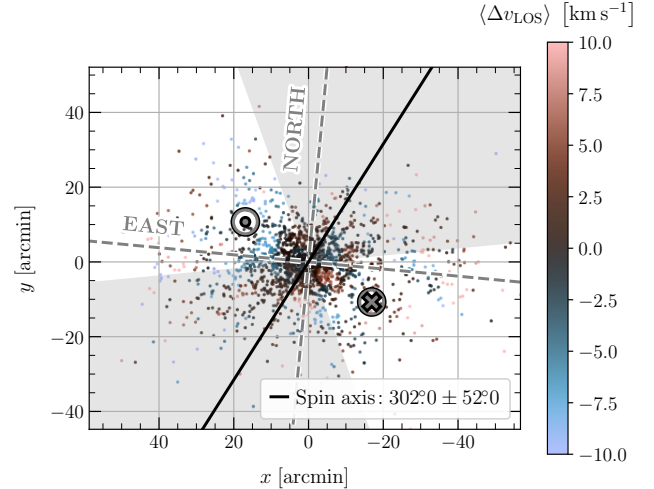


Figure 4. *Rotation:* Line-of-sight (LOS) rotation fit for Sculptor, with stars represented as scattered points, colored by the squared-error weighted mean LOS velocity, within a local circle of radius $3''.0$. The color bar is offset by the galaxy’s bulk LOS motion, such that relative receding velocities are shown in red (positive, cross symbol) and relative approaching velocities in blue (negative, dot symbol). The x - and y -axes align with the galaxy’s photometric major and minor axes, respectively, while the East and North directions are indicated with dashed gray lines. The fitted rotation axis is represented by a solid black line, with the associated $1\text{-}\sigma$ uncertainty from bootstrap realizations shown as a gray shaded region.

epochs ([Minor et al. 2010](#); [Wang et al. 2023](#); [Arroyo-Polonio et al. 2023](#)).

Following the approach in Paper I, we assess the influence of unresolved binaries on Sculptor’s dynamics by comparing LOS velocity dispersion profiles for stars grouped by their number of measured epochs. As discussed in our earlier work, if binaries contribute to inflated velocity dispersions, we would expect stars with single-epoch LOS velocity measurements to exhibit higher dispersions than those with multi-epoch measurements, where the effects of binary motion are largely averaged out ([Wang et al. 2023](#)).

Figure 3 shows that, despite Sculptor’s high binary fraction,⁸ the velocity dispersion profiles derived from stars with different numbers of epochs remain consistent within $1\text{-}\sigma$ uncertainties. This finding aligns with the previous results for Draco. We therefore conclude that Sculptor’s binary population does not introduce any bias into our mass-anisotropy estimates beyond the level of statistical uncertainties.

⁸ [Arroyo-Polonio et al. \(2023\)](#) recently estimated a binary fraction of $0.55^{+0.17}_{-0.19}$ for this dwarf galaxy.

2.2.2. Rotation

Beyond the perspective rotation due to Sculptor’s motion in the sky, which we have removed in Section 2.2, this dSph might still have residual internal rotation that can be observed through the variation of its LOS first-order velocity moments. Indeed, recent studies have suggested that Sculptor carries mild rotation in the LOS (e.g., $\langle v/\sigma \rangle = 0.15 \pm 0.15$, [Zhu et al. 2016](#)), with a spin axis aligned in between typical oblate/prolate configurations ([Arroyo-Polonio et al. 2024](#), figure 6).

While the Jeans modeling described in Section 3.1 directly accounts for the LOS first-order velocity moments, we do opt to model Sculptor as an oblate spheroid.⁹ To ensure this assumption is reasonable, we first analyze Sculptor’s rotation profile. This analysis includes determining the direction of the rotation axis and the LOS velocity amplitude along the galaxy’s photometric major axis, allowing for further comparison with our Jeans fits.

We model rotation following a similar approach to that in Paper I, by defining eight concentric annuli with linearly-spaced projected radii. For each annulus, we fit a sinusoidal function to the LOS velocity data. While each annulus is assigned an independent amplitude, we enforce a common offset and phase across all annuli to recover the bulk LOS velocity and the global spin axis, respectively. In our formalism, we first project the galaxy onto Cartesian coordinates on the sky (as in eq. 2 from [Gaia Collaboration et al. 2018](#)), and then align it with Sculptor’s major and minor axes, measuring angles clockwise from the positive x -axis (associated with an angle of 0°) to the positive y -axis.¹⁰ To better estimate the uncertainties in our fits, we employ a bootstrap methodology with 10,000 realizations.

Figure 4 shows the fitted rotation axis direction alongside a smoothed map of LOS velocities for the stars included in our modeling. We determine a rotation axis direction of $\phi_0 = 302^\circ 0 \pm 52^\circ 0$, consistent with an oblate configuration (i.e., $\phi_0 = 270^\circ 0$). This result is in good agreement with recent estimates by [Arroyo-Polonio et al. \(2024\)](#), whose spin axis direction, expressed within our formalism, corresponds to $331^\circ 4 \pm 18^\circ 0$. The rotation amplitude along the photometric major axis is presented later in Figure 7 together with our PM data, but a brief look reveals a modest but non-negligible rotation signal of $\sim 2 \text{ km s}^{-1}$, which

⁹ The Jeans modeling code we use, JAMPY, is currently designed to handle either oblate or prolate configurations, but not intermediate arrangements.

¹⁰ For Sculptor, these directions approximately align with the East and North directions, respectively.

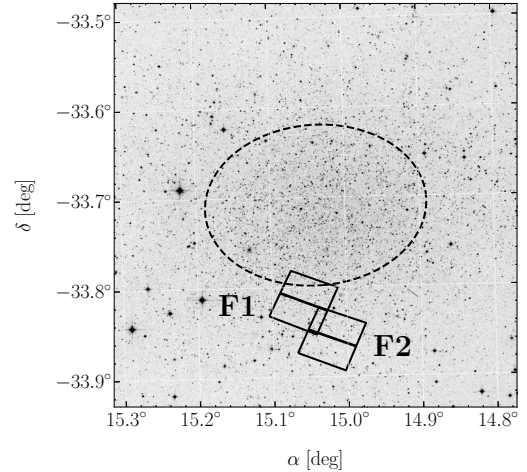


Figure 5. *Observed fields:* *HST* target fields (background image is from the STScI Digitized Sky Survey, see acknowledgments), with a black ellipse showing Sculptor’s half-number radius.

amounts to approximately 20% of Sculptor’s internal velocity dispersion. This low rotation amplitude also explains why the rotation axis direction remains poorly constrained in our fits.

2.3. Proper Motions

2.3.1. Observations and Astrometric Catalogs

For our new PM measurements of Sculptor stars, we utilized multi-epoch *HST* ACS/WFC imaging data. Details about the field locations and earlier epoch observations for our target fields, F1 and F2, are provided in [Sohn et al. \(2017\)](#). The locations of these fields are also shown in Figure 5. In brief, both fields had two epochs of imaging data obtained in 2002 and 2013. Both 2002 and 2013 observations were performed using the F775W filter, and for 2013 observations, an additional filter F606W was used to create CMDs. These fields were revisited in October 2022 and October 2023 through our *HST* program GO-16737 ([Sohn et al. 2021](#)), using the same telescope pointing and orientation as in the previous epochs. During this latest epoch, we acquired 12 individual exposures using the F775W filter for each field, with each exposure lasting 495 seconds.

Data analysis largely followed the procedures outlined in [Bellini et al. \(2018\)](#), [Libralato et al. \(2018\)](#), and Paper I. Here, we provide a high-level summary of the PM derivation process and refer the reader to those works for methodological details. We downloaded the flat-fielded `flt.fits` images for all target fields and epochs from the Mikulski Archive for Space Telescopes (MAST). These were processed using the `hst1pass` program ([Anderson 2022](#)) to derive positions and fluxes for each star in every exposure. Instead of using the

`_flc.fits` images, which are corrected for charge transfer efficiency (CTE) losses, we employed the table-based CTE correction option in `hst1pass`. This is an improved version of the corrections used in earlier works (Anderson 2022; Anderson, in prep.). Positional corrections were applied using the ACS/WFC geometric distortion solutions from Kozhurina-Platais et al. (2015), further extended to account for time-dependent distortion variations beyond 2020 (V. Kozhurina-Platais, private communication).

For each field, a “master frame” was constructed using the average positions of stars from the repeated first-epoch exposures. The (X, Y) axes of these master frames were aligned to (α, δ) coordinates by registering stellar positions to the *Gaia* DR3 astrometric system. Positions of stars from subsequent epochs were aligned to these master frames using a six-parameter linear transformation, and average positions were computed for each epoch. This procedure inherently aligns the star fields across epochs, resulting in zero PM on average for Sculptor dSph stars. Since our focus is on measuring internal velocity dispersion in the plane of the sky, this alignment does not affect our results. Uncertainties on average positions were determined as the root mean square of repeated measurements divided by the square root of the number of exposures. Finally, for each field and epoch, we prepared a catalog containing star positions as derived above, along with average instrumental magnitudes¹¹ in F606W and F775W (from previous epochs), as output by `hst1pass`.

2.3.2. Photometric Cleaning & Local Corrections

With the catalogs catalogs of star positions, we compute raw PMs through a least-squares line fit of the master frame (X, Y) positions as a function of the epoch time. We use the `POLYFIT` routine from `NUMPY` (van der Walt et al. 2011), assuming measured (X, Y) uncertainties, and no χ^2 re-scaling. Next, the procedures for cleaning the photometry, removing CMD outliers, and applying local PM corrections to account for *HST* systematics followed the methodology outlined in Paper I (sections 2.3.2 and 2.3.3). Below, we briefly summarize the key steps, which are applied independently to each field.

1. We begin by identifying and removing clear outliers in the CMD and in the magnitude-QFIT¹² diagrams, employing a friends-of-friends algorithm.

¹¹ The instrumental magnitude in a given filter is defined as $\text{mag} = -2.5 \log c$, where c is the electron count per exposure for a source.

¹² QFIT quantifies a combined measure of goodness-of-fit and S/N; see Anderson et al. (2006); Libralato et al. (2014) for details.

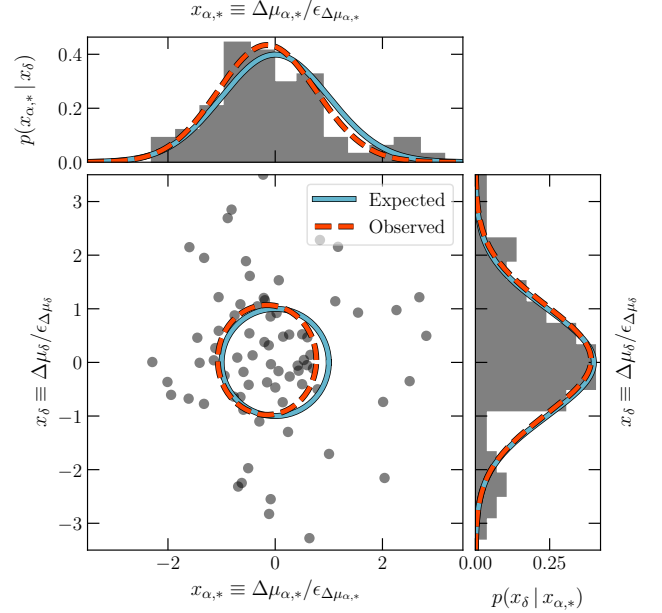


Figure 6. *Validation of local corrections:* Histogram of proper motion differences for matched stars in overlapping fields, derived from an independent correction process for *HST* systematics and normalized by the combined error budget propagated through our procedure. Each axis corresponds to the normalized difference in one of the proper motion components, $\mu_{\alpha,*}$ or μ_{δ} . The dashed-red curve represents a Gaussian constructed using median-based statistics, accounting for low-number statistics and the absence of data cleaning. This is compared with the expected normal distribution for a well-behaved dataset, shown in blue. The agreement between the curves demonstrates the effectiveness of our local corrections, as detailed in Section 2.3.2.

2. Next, we address *HST* instrument systematics, which often appear as spatially-correlated mean motions of stars across different regions of the telescope detectors (e.g. Bellini et al. 2018; Libralato et al. 2018). To correct for this, we calculate and apply median-based shifts, with uncertainties propagated to both PM directions, using a local network of neighboring stars.
3. The effectiveness of these corrections is validated through diagnostic checks, such as reproducing the equivalent of figure 8 from Paper I. This process effectively removes first-order velocity moments, such as rotation or global streaming motions, while preserving the second-order moments necessary for accurate mass-anisotropy modeling. We also test the impact of this data manipulation later on Section 5.2.1.

A key feature of our new data is that, while each field is initially processed independently, they include over-

lapping regions, as shown in Figure 5. This intersection allows for a direct comparison of matched stars. If the local corrections are effective and properly applied, the overall PM differences between matched stars should be consistent with their associated PM uncertainties and should not exhibit significant systematic shifts. Specifically, the distribution of PM differences, normalized by their combined error budget, is expected to approximate a Gaussian distribution with a mean of zero and a standard deviation of one.

To test this, we account for the non-Gaussian nature of the datasets, arising primarily from two factors: the absence of error cleaning in this initial subset of matched stars and the low-number statistics. These factors can influence the distribution of PM differences, potentially introducing asymmetries or heavier tails. To address these issues, we employ median-based statistics to constrain the center and spread of the data. Specifically, we define

$$x_i \equiv \Delta\mu_i / \epsilon_{\Delta\mu_i}, \quad (1)$$

where the suffix i stands for $\alpha, *$ or δ ¹³ and ϵ is used to refer to uncertainties, rather than the σ symbol used for the standard deviation. Next, we use the median and the median absolute deviation (MAD) of the x_i distribution to construct a corresponding Gaussian curve. The MAD, corrected to account for Gaussian standard deviations as defined in Beers, Flynn, & Gebhardt (1990), is

$$\text{MAD} = \frac{\eta_{50}(|x - \eta_{50}(x)|)}{0.6745} \quad (2)$$

where $\eta_{50}(x)$ refers to the 50th percentile (i.e., the median) of the distribution of x .

Figure 6 compares the Gaussian curve computed using the median and MAD (shown in red) with the expected normal distribution (shown in blue). The agreement between these two curves supports the validity of the local corrections applied to our PM dataset. Not only are the PM differences not significantly shifted toward positive or negative values, but the propagated uncertainties also adequately encompass the observed spread in the data. As a further check, we also performed this analysis using a skewed Gaussian fit,¹⁴ finding that the resulting mean and dispersion remained consistent with those of the expected normal distribution. Following this validation, we proceed to the next stage, which involves cleaning stars with high PM errors and removing outliers in PM.

¹³ Hereafter, $\alpha, *$ refers to the component $\mu_{\alpha,*} = (d\alpha/dt) \cos \delta$ from the PM vector.

¹⁴ This test was motivated by the prominent tail towards $(x_{\alpha,*}, x_{\delta}) \sim (2.5, -2.5)$ visible in Figure 6.

2.3.3. Outliers and Underestimated Errors

Before constructing PM profiles, we perform a final round of data cleaning for our PM measurements, guided by the analyses presented in Paper I. Specifically, we compute the global velocity dispersion¹⁵ of our PM dataset for each field, applying various thresholds for the maximum allowable PM uncertainty. We select the highest threshold that meets two criteria: (i) it remains within the same order of magnitude as the expected LOS velocity dispersion, for a given distance, and (ii) it lies in a plateau of velocity dispersions before increasing due to likely underestimated errors. As discussed in detail in Paper I and prior works (e.g., Watkins et al. 2015; Vitral et al. 2022), this step is critical for accurate mass modeling. Indeed, underestimated errors, when exceeding the intrinsic velocity dispersion, can introduce significant biases into equilibrium-based mass measurements.

Based on this, we adopt a threshold of $\epsilon_{\mu} < 0.023 \text{ mas yr}^{-1}$ on the PM error;¹⁶ stars with larger errors are excluded from the subsequent analysis. Additionally, we apply a $3\text{-}\sigma$ outlier cut, as in Paper I. We once again use median-based statistics (median and MAD) rather than the nominal mean and standard deviation to ensure robustness against outliers.¹⁷ Finally, we treat matched stars from overlapping fields as single entries, following a similar approach to the merging of our LOS datasets (i.e. using the weighted mean of the individual measurements). The resulting PM catalog for Sculptor comprises 119 stars with PM uncertainties below its intrinsic velocity dispersion, representing the most accurate PM dataset ever assembled for this dwarf galaxy.

2.3.4. Proper Motion Dispersion Profiles

With our new PM dataset, we present for the first time in Figure 7 the radially-resolved transverse velocity dispersion profiles of the Sculptor dSph. Although these profiles are less spatially extended than those shown for Draco in Paper I, they remain valuable for breaking degeneracies between the galaxy’s mass distribution and orbital structure – that is, the velocity anisotropy, which

¹⁵ Here and throughout this work, the dispersion of a discrete dataset with uneven uncertainties is computed as described in appendix A of van der Marel & Anderson (2010), a procedure thoroughly validated in multiple works (e.g., Watkins et al. 2015; Vitral et al. 2023a and Paper I).

¹⁶ This translates to a transverse velocity of 9.4 km s^{-1} , for a given distance of 85.8 kpc (cf. Table 2).

¹⁷ Note that this step mainly serves to exclude stars too far from the galaxy’s bulk motion; in practice, only one of the stars removed lay within $5\text{-}\sigma$ from the median.

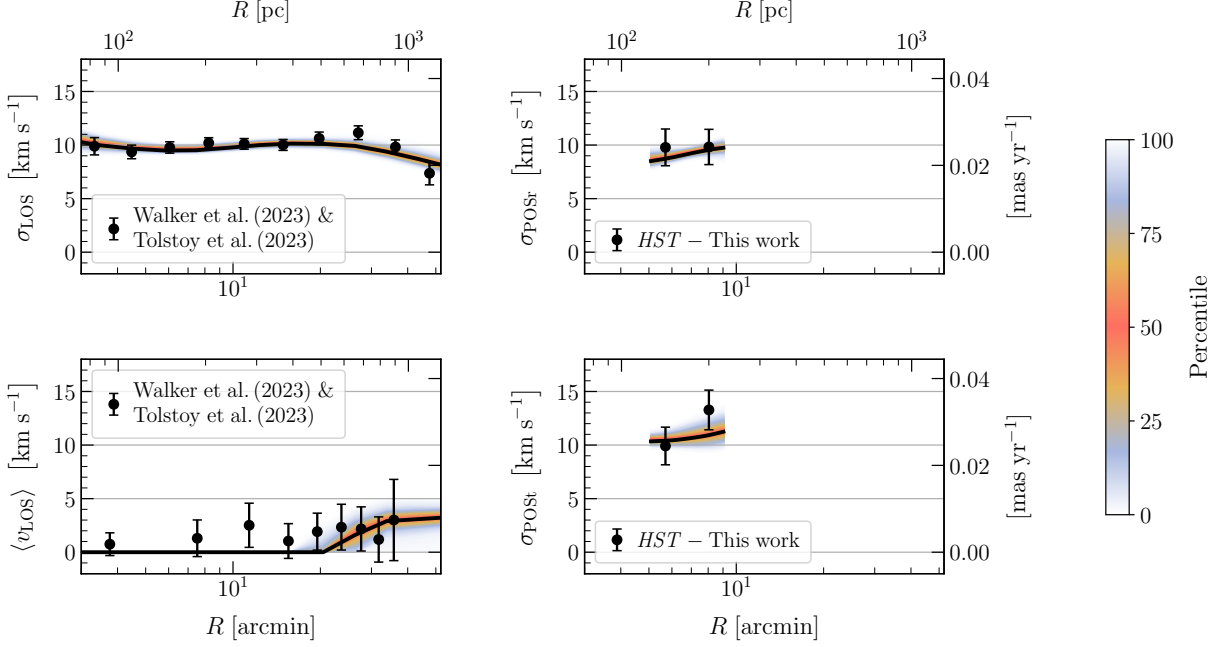


Figure 7. *Radially dependent kinematics:* Setup of the kinematic data used in our Jeans modeling, shown as black dots. While binned profiles are displayed for clarity, the modeling uses a likelihood approach on a discrete dataset. The upper and lower left panels show the angularly averaged line-of-sight velocity dispersion and major-axis first-order moment computed with data from Walker et al. (2023) and Tolstoy et al. (2023). The upper and lower right panels show the radial and tangential transverse velocity dispersions from our *HST* programs, over the fields in Figure 5. Solid black lines and shaded regions mark the median and posterior percentiles of our Jeans fits for a fiducial inclination of 57° , also used to convert proper motions to velocities in the rightmost panel. Model curves are interpolated over the projected radius R for visualization, though they also vary with projected angle.

describes whether the stellar orbits are preferentially radial or tangential.

Quantitatively, we find a ratio of tangential to radial PM dispersions of $\langle\sigma_{\text{POSt}}\rangle / \langle\sigma_{\text{POSr}}\rangle = 1.19 \pm 0.19$ across the spatial extent of the data, where POSr and POSt refer to the plane-of-sky radial and tangential directions, respectively. The ratio of LOS to PM dispersions is $\langle\sigma_{\text{LOS}}\rangle / \langle\sigma_{\text{POS}}\rangle = 0.93 \pm 0.08$, with σ_{POS} denoting the average dispersion over both transverse directions. The former ratio is independent of the galaxy’s distance, while the latter scales inversely with it.¹⁸

These measurements place important constraints on Sculptor’s internal velocity structure, particularly on its velocity anisotropy. As discussed in Sections 3 and 4, the relative values of the velocity dispersions in different directions – captured here by ratios such as $\langle\sigma_{\text{POSt}}\rangle / \langle\sigma_{\text{POSr}}\rangle$ and $\langle\sigma_{\text{LOS}}\rangle / \langle\sigma_{\text{POS}}\rangle$ – provide strong leverage for disentangling the orbital structure and intrinsic shape of the galaxy.

3. METHODS

3.1. Axisymmetric Jeans Modeling: JAMPY

As in Paper I, we use the mass anisotropy modeling code JAMPY (Cappellari 2020), configured such that the velocity ellipsoid aligns with spherical coordinates. This choice follows our assumption of a spherical DM potential, which is expected to dominate the system’s dynamics when compared to Sculptor’s luminous axisymmetric component. In this configuration, JAMPY applies the Jeans equations for rotating axisymmetric systems (e.g., Bacon, Simien, & Monnet 1983),

$$\frac{\partial(\nu \langle v_r^2 \rangle)}{\nu \partial r} + \frac{(1 + \beta_J) \langle v_r^2 \rangle - \langle v_\phi^2 \rangle}{r} = -\frac{\partial \Phi}{\partial r}, \quad (3a)$$

$$\frac{(1 - \beta_J)}{\nu} \left[\frac{\partial(\nu \langle v_r^2 \rangle)}{\partial \theta} + \frac{\nu \langle v_r^2 \rangle}{\tan \theta} \right] - \frac{\langle v_\phi^2 \rangle}{\tan \theta} = -\frac{\partial \Phi}{\partial \theta}, \quad (3b)$$

where Φ is the gravitational potential, and $\langle \cdot \rangle$ denotes the distribution function-averaged quantity. The anisotropy parameter β_J , assumed to be independent of θ , is given by

$$\beta_J \equiv 1 - \frac{\langle v_\theta^2 \rangle}{\langle v_r^2 \rangle} = 1 - \frac{\sigma_\theta^2}{\sigma_r^2}, \quad (4)$$

¹⁸ The quoted value assumes $D = 85.83$ kpc, as predicted by our Jeans fits in the final row of Table 2.

where the second equality assumes $\langle v_\theta \rangle = \langle v_r \rangle = 0$. Due to symmetry and continuity, axisymmetric models always satisfy $\langle v_\phi \rangle = 0$ and $\langle v_\phi^2 \rangle = \langle v_\theta^2 \rangle$ along the symmetry axis. Consequently, along this axis, the anisotropy parameter β_B , as defined by Binney (1980),

$$\beta_B \equiv 1 - \frac{\langle v_\theta^2 \rangle + \langle v_\phi^2 \rangle}{2 \langle v_r^2 \rangle}, \quad (5)$$

equals β_J . Models with $\beta_J = 0$ yield the same predicted second velocity moments as models in which the distribution function $f(E, Lz)$ does not depend on a third integral. Such models have been widely used for fitting data of axisymmetric systems (e.g. van der Marel 1991). Away from the symmetry axis, models with $\beta_J = 0$ do *not* have an isotropic velocity dispersion tensor.

By not enforcing $\langle v_\phi \rangle = 0$ throughout the entire system, JAMPY allows users to model rotation in the fitted galaxy – a feature often neglected in previous kinematic models of Sculptor (e.g., Massari et al. 2017; Hayashi et al. 2020). The first moment in the ϕ direction is related to the second-order moment in the radial direction through

$$\langle v_\phi \rangle^2 = \langle v_\phi^2 \rangle - \sigma_\phi^2, \quad (6a)$$

$$\sigma_\phi^2 = (1 - \Omega) \langle v_r^2 \rangle, \quad (6b)$$

where Ω is the rotation parameter, also assumed to be independent of θ . This parameter was denoted as γ in Cappellari (2020), but we adopt a different notation here to avoid confusion with the inner slope of the DM mass density, which is commonly represented by the same symbol.

From the solutions to these equations, JAMPY calculates projected velocity moments, which we then use to compute the respective quantities in the LOS and POS directions. We sample the parameter space using the Markov Chain Monte Carlo (MCMC) sampler EMCEE (Foreman-Mackey et al. 2013), by using a likelihood \mathcal{L} defined as

$$\mathcal{L} = \prod_{i, \text{LOS}} G_{\text{LOS}}(v_{\text{LOS}, i}) \times \prod_{i, \text{POS}} G_{\text{POSr}}(\mu_{\text{POSr}, i}) G_{\text{POS}\theta}(\mu_{\text{POS}\theta, i}). \quad (7)$$

With respect to equation 7, a few key considerations must be clarified:

- $G(x)$ represents a Gaussian function of argument x .

- Since the stars with PMs in our dataset do not have a corresponding v_{LOS} measurement,¹⁹ the product of the POS Gaussian components can be effectively treated separately from the LOS Gaussian component, with no risk of neglecting cross-terms in spherical or axisymmetric symmetry.
- For all Gaussian components, the respective standard deviation is derived from the output of JAMPY along the corresponding dimension, using the relation $\sigma^2 = \langle v^2 \rangle - \langle v \rangle^2$. To this, we add the individual stellar errors quadratically, assuming Gaussian-distributed uncertainties.
- For the LOS component, the Gaussian mean is taken as the bulk LOS motion of Sculptor, plus the respective first-order moment estimated by JAMPY, and adjusted to the pre-defined sense of rotation in Sculptor. For the POS components, however, we adopt a null mean as a result of our local cleaning process explained in Section 2.3.2, which effectively removes streaming motions in our PMs.
- Although the assumption of Gaussian-distributed projected velocities is formally incorrect in the presence of anisotropy (Merritt 1987, figure 8), we retain it due to the demonstrated convergence of this approach when applied to mock datasets generated by self-consistent distribution functions (Read et al. 2021), as well as its consistency with results from well-studied dynamical systems (see Watkins et al. 2013, for an application to ω Centauri).

Throughout our posterior sampling, we employ priors as defined in Section 3.1.1. Our MCMC routine is configured to run a minimum of 20 000 steps per fit,²⁰ and we execute the runs in parallel on the local cluster at the University of Edinburgh. In these configurations, each run takes approximately 3 days to complete. We repeat the process for a different set of possible inclinations, drawn from the PDF derived in Section 2.1. To discard the burn-in phase, we remove the first 75% of the steps from each chain and visually check that the chains remain stable thereafter.

¹⁹ This is because our *HST* exposures target the more numerous faint stars, while the brighter stars for which ground-based spectroscopic measurements are typically possible are often saturated in the respective *HST* images.

²⁰ If proper convergence is not achieved, we add an additional 10 000 steps, which was sufficient in our case.

3.1.1. Parametrizations & Priors of JAMPY

Our parametrization follows the approach of Paper I. The baryonic content is fixed and modeled with a flattened Plummer profile, with parameters determined in Section 2.1. Owing to the lack of external constraints on the halo shape, the DM halo is modeled as a spherical generalized Plummer profile,²¹ with a steeper outer slope ($\beta = 5$) motivated by tidal interactions inferred from Sculptor’s orbital history (Sohn et al. 2017), consistent with the findings of Peñarrubia et al. (2010). This DM parametrization was also adopted in Paper I, Hayashi et al. (2020), and Goldstein & Strigari (2025).

This density model depends on three parameters: a scale radius r_{dark} , a total DM mass (M_{dark}), and an inner slope γ_{dark} . We assume flat/log-flat priors for all of these variables,

- $\gamma_{\text{dark}} \in [-2, 2]$, which includes both cuspy ($\gamma = -1$) and cored ($\gamma = 0$) profiles. We allow for positive slopes to account for potential physical mechanisms not necessarily anticipated by Λ CDM.
- $\log(M_{\text{dark}}/[M_{\odot}]) \in [6, 12]$. Read et al. (2017) extrapolated classical $M_{\star} - M_{200}$ relations to lower-mass dSphs, such that Sculptor, with a luminous mass of $\sim 8.08 \times 10^6 M_{\odot}$, should have $M_{200} \sim 10^9 M_{\odot}$. Therefore, our priors largely cover this range.
- $\log(r_{\text{dark}}[\text{kpc}]) \in [-1, 2]$. Given the expected M_{200} mass from Read et al. (2017),²² the concentration relation from Dutton & Macciò (2014) yields a Navarro et al. (1997) profile scale radius of nearly 2 kpc. Our prior thus covers this with more than an order of magnitude range.

We assume that the anisotropy parameters, β_J and Ω , are constant and fit their symmetrized quantity,²³ defined as $x_{\text{sym}} = x/(1 - x/2)$, using a flat prior between -1.99 and 1.99 . To assess the impact of this assumption, we have separately tested variations with a radial dependence, such as generalized parametrizations (Osipkov 1979; Merritt 1985), and found no significant effect on our results and conclusions presented further on.

Finally, we apply Gaussian priors for the bulk v_{LOS} of Sculptor, setting $v_{\text{LOS}} = 111.2 \pm 0.3 \text{ km s}^{-1}$ (Arroyo-Polonio et al. 2024), and for the distance modulus,

²¹ A special case of the $\alpha\beta\gamma$ profile (Zhao 1996), with $\alpha = 2$, $\beta = 5$, and a free inner slope γ (see eq. A3 from Paper I).

²² We thank Justin Read for sharing his algorithm to compute the precise M_{200} value expected for Sculptor.

²³ x_{sym} ranges monotonically from -2 to $+2$, given that x spans similarly from $-\infty$ to $+1$.

defined as $\mu_0 = 5 \log(D[\text{kpc}]) + 10$. We adopt $\mu_0 = 19.67 \pm 0.05$, which is the weighted mean of measurements reported in (Rizzi 2002, RGB and TRGB), (Pietrzyński et al. 2008, RR-Lyrae on V and I bands), and (Górski et al. 2011, TRGB on J and K bands).

3.2. Practical Quantities

As in Paper I, we compute derived quantities to better interpret the results of our fits, as some quantities can be difficult to assess in their original form. For instance, due to the mass-anisotropy degeneracy, constraining the asymptotic DM density slope is particularly challenging in the absence of 3D velocities near the galaxy center. Instead, a more meaningful approach is to evaluate the DM density slope within the radial range where both PMs and LOS velocities are available. We define this as an effective DM slope:

$$\Gamma_{\text{dark}} \equiv \frac{\int_{r_{\text{min}}}^{r_{\text{max}}} \frac{d \log \rho}{d \log r} \rho(r) dr}{\int_{r_{\text{min}}}^{r_{\text{max}}} \rho(r) dr}, \quad (8)$$

where $\rho(r)$ is the DM density. The lower bound, r_{min} , corresponds to the smallest projected radius in the data where PM information is available. We set the upper bound as $r_{\text{max}} = \min(R_{\text{max,PM}}, r_{\Lambda\text{CDM}}/3)$, where $R_{\text{max,PM}}$ is the largest projected radius with available PM data, and $r_{\Lambda\text{CDM}}$ is the NFW scale radius expected for DM halos in Λ CDM simulations.²⁴ (computed with the relations from Read et al. 2017).

Additionally, as in our previous work, we compute the circular velocity:

$$v_{\text{circ}}(r) = \sqrt{\frac{GM(r)}{r}}, \quad (9)$$

which depends on the total²⁵ cumulative mass enclosed within radius r and the gravitational constant G .

4. RESULTS

We ran JAMPY over a set of eleven inclinations, linearly spaced from $43^\circ.7$ to 90° (edge-on), covering the range of Sculptor’s inclination PDF computed in Section 2.1, to mimic the analyses from Paper I. The results are presented in Table 2. In addition to the anisotropy parameter β_J , defined in Eq.(4), we also report the

²⁴ We adopt this reference value to facilitate comparison with theoretical predictions. The factor $(1/3)$ is introduced to exclude the region where the density profile steepens due to the transition from the inner to outer profile.

²⁵ The total mass includes both luminous and dark components.

Table 2. Main results of the JAMPY axisymmetric Jeans modeling.

i	D	Ω	β_J	r_{dark}	$M_{\text{dark}}^{R_{\text{max}}}$	γ_{dark}	Γ_{dark}	$\overline{\beta_B}$	$v_{\text{circ}}^{R_{\text{max}}}$
[°]	[kpc]			[10^2 pc]	[$10^8 M_\odot$]				[km s^{-1}]
(1)	(2)	(3)	(4)	(5)	(6)	(7)	(8)	(9)	(10)
43.7	$87.69^{+1.92}_{-1.96}$	$-2.20^{+0.32}_{-0.37}$	$0.98^{+0.00}_{-0.00}$	$3.32^{+0.55}_{-0.32}$	$1.68^{+0.16}_{-0.14}$	$1.35^{+0.45}_{-0.62}$	$-0.16^{+0.15}_{-0.20}$	$0.94^{+0.00}_{-0.00}$	$20.79^{+0.87}_{-0.79}$
47.7	$85.98^{+1.94}_{-1.94}$	$-0.53^{+0.19}_{-0.20}$	$0.92^{+0.01}_{-0.01}$	$4.26^{+0.42}_{-0.32}$	$2.11^{+0.25}_{-0.21}$	$1.64^{+0.23}_{-0.45}$	$0.52^{+0.19}_{-0.22}$	$0.82^{+0.02}_{-0.03}$	$23.49^{+1.13}_{-1.26}$
52.4	$85.79^{+2.40}_{-1.88}$	$-0.42^{+0.26}_{-0.24}$	$0.86^{+0.03}_{-0.03}$	$4.49^{+0.69}_{-0.42}$	$2.04^{+0.24}_{-0.27}$	$1.58^{+0.28}_{-0.37}$	$0.57^{+0.19}_{-0.20}$	$0.68^{+0.06}_{-0.07}$	$22.80^{+1.49}_{-1.26}$
57.1	$85.46^{+2.07}_{-1.81}$	$-0.91^{+0.45}_{-0.75}$	$0.72^{+0.07}_{-0.12}$	$4.06^{+0.65}_{-0.51}$	$1.50^{+0.32}_{-0.30}$	$1.45^{+0.41}_{-0.68}$	$0.29^{+0.31}_{-0.41}$	$0.35^{+0.17}_{-0.39}$	$19.88^{+1.97}_{-1.93}$
61.8	$85.78^{+1.79}_{-1.92}$	$-4.76^{+3.08}_{-4.75}$	$-0.10^{+0.60}_{-1.06}$	$6.37^{+10.14}_{-2.64}$	$0.95^{+0.25}_{-0.17}$	$-1.12^{+2.09}_{-0.75}$	$-1.39^{+1.18}_{-0.51}$	$-1.04^{+0.99}_{-2.15}$	$16.05^{+1.89}_{-1.42}$
66.5	$85.73^{+1.75}_{-1.73}$	$-6.35^{+2.64}_{-2.89}$	$-0.79^{+0.71}_{-0.67}$	$12.17^{+60.81}_{-5.82}$	$0.90^{+0.23}_{-0.18}$	$-1.78^{+0.65}_{-0.15}$	$-1.83^{+0.44}_{-0.13}$	$-1.91^{+1.36}_{-1.39}$	$15.67^{+1.77}_{-1.52}$
71.2	$85.69^{+2.02}_{-2.01}$	$-5.42^{+2.83}_{-2.65}$	$-0.60^{+0.72}_{-0.65}$	$9.64^{+27.90}_{-4.84}$	$0.88^{+0.18}_{-0.16}$	$-1.65^{+1.10}_{-0.28}$	$-1.74^{+0.69}_{-0.21}$	$-1.92^{+1.34}_{-1.10}$	$15.47^{+1.46}_{-1.37}$
75.9	$85.28^{+1.87}_{-1.86}$	$-5.48^{+1.91}_{-2.40}$	$-0.77^{+0.55}_{-0.57}$	$13.05^{+51.39}_{-6.06}$	$0.88^{+0.18}_{-0.18}$	$-1.79^{+0.50}_{-0.16}$	$-1.85^{+0.34}_{-0.12}$	$-2.22^{+1.04}_{-0.93}$	$15.56^{+1.35}_{-1.57}$
80.6	$85.48^{+1.82}_{-1.83}$	$-5.71^{+1.83}_{-5.48}$	$-0.83^{+0.54}_{-0.50}$	$15.02^{+104.45}_{-7.24}$	$0.88^{+0.18}_{-0.18}$	$-1.84^{+0.42}_{-0.11}$	$-1.87^{+0.29}_{-0.09}$	$-2.18^{+1.00}_{-0.88}$	$15.48^{+1.45}_{-1.53}$
85.3	$85.45^{+1.84}_{-1.76}$	$-5.83^{+1.81}_{-11.00}$	$-0.88^{+0.48}_{-0.47}$	$16.18^{+93.35}_{-7.63}$	$0.89^{+0.16}_{-0.19}$	$-1.87^{+0.33}_{-0.09}$	$-1.90^{+0.24}_{-0.08}$	$-2.25^{+1.14}_{-0.91}$	$15.62^{+1.21}_{-1.22}$
90.0	$85.53^{+1.90}_{-1.81}$	$-5.47^{+1.79}_{-4.00}$	$-0.86^{+0.50}_{-0.51}$	$16.64^{+173.46}_{-8.33}$	$0.90^{+0.18}_{-0.19}$	$-1.86^{+0.36}_{-0.10}$	$-1.88^{+0.25}_{-0.09}$	$-2.16^{+1.23}_{-0.98}$	$15.65^{+1.40}_{-1.66}$
$\langle \cdot \rangle_i$	$85.83^{+2.02}_{-1.91}$	$-3.16^{+1.75}_{-4.96}$	$0.13^{+0.78}_{-1.15}$	$7.86^{+8.51}_{-7.86}$	$1.39^{+0.68}_{-0.58}$	$-0.02^{+1.76}_{-1.82}$	$-0.67^{+1.23}_{-1.24}$	$-0.56^{+1.33}_{-2.00}$	$18.88^{+4.23}_{-3.94}$

NOTES – Columns are (1) Inclination, in degrees (90° is edge-on); (2) Heliocentric distance, in kpc; (3) Rotation parameter (see Eq. [6]); (4) β_J velocity anisotropy parameter, as defined in Eq. (4); (5) Dark matter scale radius, in 10^2 pc; (6) Dark matter mass at maximum projected data radius, in $10^8 M_\odot$; (7) Dark matter asymptotic density slope; (8) Dark matter density slope averaged over the spatial range where PMs are available; (9) Globally-averaged β_B velocity anisotropy, as defined in Eq. (5); (10) Circular velocity at maximum projected data radius, in km s^{-1} . The uncertainties are based on the 16th and 84th percentiles of the marginal distributions. The last row displays the integrated estimate for each parameter, averaged over the inclination probability distribution of Sculptor, as described in Section 4.1.

globally-averaged Binney anisotropy, $\overline{\beta_B}$. The latter is computed by first determining the stellar-mass-weighted second velocity moments, averaged over the entire system, and then substituting them into Eq.(5).

4.1. Inclination Dependence

Regarding the dependence of model parameters on the adopted galaxy inclination, Paper I found that, while correlations were present, Draco’s overall parameters remained relatively consistent. That is, the parameters largely retained their signs, preserving the general regime they indicated (e.g., velocity anisotropy remained tangential, and the DM slope differed from the cored case across all inclinations).

In this study, we observe similar correlations with inclination; however, their impact on our modeling conclusions is much more pronounced. Specifically, the best-fitting flattened systems exhibit extreme radial anisotropy with a corresponding steep density drop, whereas the best-fitting edge-on systems exhibit extreme tangential anisotropy with a corresponding highly-cuspy density profile. This diversity of DM slopes is showcased in Figure 8.

The inclination-averaged best-fit parameters of our model were computed using the inclination PDF shown in Figure 2, following the formalism presented in Pa-

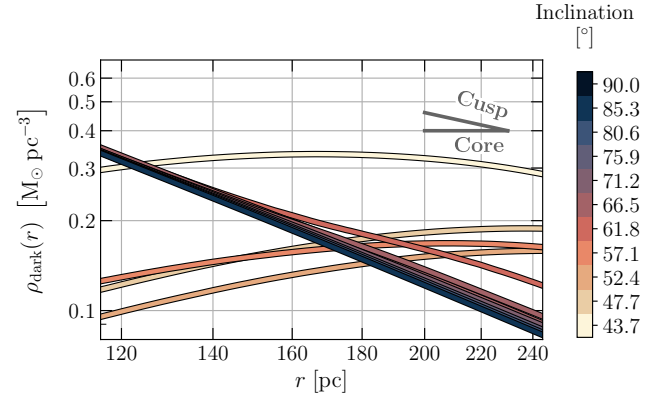


Figure 8. *Degeneracy with inclination:* Best-fitting dark matter density profiles within the radial range constrained by the three-dimensional velocity data, shown alongside reference slopes representative of core and cusp profiles. Each color corresponds to a tested inclination drawn from Sculptor’s inclination probability distribution function. The figure illustrates a pronounced degeneracy between the dark matter density slope and the assumed inclination – an effect that is overlooked under the assumption of spherical symmetry.

per I, Section 4.2.1. As expected from the strong degeneracy discussed above, the DM slope and velocity anisotropy are well constrained only for specific inclination values, but not in the averaged case. This result

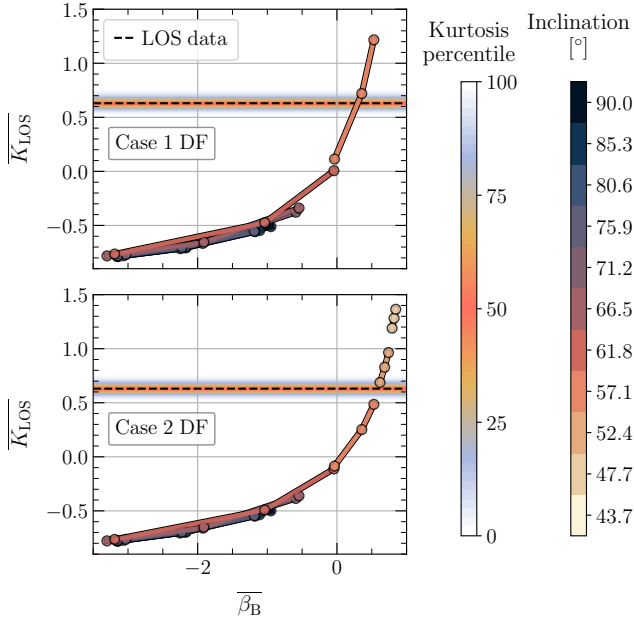


Figure 9. *Higher-order moments:* Spatially-averaged kurtosis of the line-of-sight velocity distribution as a function of the averaged velocity anisotropy β_B , defined in eq. 5. The two panels correspond to different distribution functions explored by the SCALEFREE software from de Bruijne et al. (1996). The observed kurtosis distribution from our LOS velocity data is shown using the color scale on the left, with the dashed black line marking its mean. For each distribution function and inclination (color scale on the right), we compute the corresponding SCALEFREE-predicted kurtosis using three representative values of β_B : the 16th percentile, the median, and 84th percentile (from Table 2, column 9), shown as connected points. The figure illustrates a consistent preference for less inclined (i.e., more flattened) configurations of the Sculptor dSph, regardless of the adopted distribution function.

highlights the critical role of properly accounting for inclination in the mass modeling of flattened systems.

4.1.1. Higher-order velocity moments

When first-order velocity moments are available in all three dimensions, the inclination of an axisymmetric system can be directly constrained using relations like those in Evans & de Zeeuw (1994, eq. [A4]) or via Jeans modeling with the inclination as a free parameter. However, correcting systematic effects in *HST*-based proper motions (as detailed in Section 2.3.2) removes transverse first-order moments by design. Our Jeans analysis thus relies solely on the LOS first-order moment, which is insufficient to determine inclination on its own.

To address this degeneracy, we turn to the SCALEFREE models of de Bruijne et al. (1996), further detailed in Paper I (appendix B). These models assume an axisymmet-

ric baryonic component in a spherical potential²⁶ and, by adopting fiducial distribution functions and potential forms, offer a reasonable and generalized approximation of systems like dSphs with flattened dispersion profiles. While these models do not capture the detailed radial variation of the logarithmic density and potential slope, they can, unlike Jeans modeling, use higher-order moments of a single velocity dimension (here, LOS) to break degeneracies between mass, anisotropy, and crucially, inclination. This offers educated guesses of the inclination via features such as the kurtosis of the LOS velocity distribution (e.g., Paper I, fig. 18).

Following this approach, we compute the observed LOS kurtosis to be $\overline{K}_{\text{LOS}} = 0.63 \pm 0.05$ and compare it to SCALEFREE predictions across a range of inclinations, using our inferred velocity anisotropies. Figure 9 shows two panels, one per SCALEFREE distribution function type, with the observed kurtosis distribution color-coded as in the leftmost color bar, and its mean marked by a dashed black line. For each inclination, we compute the expected kurtosis from SCALEFREE using three representative values of the average velocity anisotropy β_B : the 16th percentile, the median, and the 84th percentile (from Table 2, column 9).

In both distribution function cases, the models favor lower inclinations (i.e., more flattened systems). The first panel yields the best match²⁷ at $i = 57^\circ.1$, with the second at $i = 52^\circ.4$. Although these generalized SCALEFREE-based models are not designed for precise inclination fitting, the consistent need for radial velocity anisotropy to match the observed kurtosis supports the idea that Sculptor lies toward the more flattened end of the viable axial ratio range. This result remains robust even under conservative 3- and 4- σ clipping of the LOS velocity distribution.

4.2. Data-Model Comparison

While having in mind the degeneracies in our dataset and the inclination-averaged estimates summarized in the last row of Table 2, adopting a Jeans model tied to a fiducial inclination offers a clearer benchmark for comparing data and interpreting results. For this purpose, we adopt the $i = 57^\circ.1$ Jeans model as our fiducial setting, as it corresponds both to the best SCALEFREE match under its distribution function of type 1 and approximates the median inclination of the posterior shown in Figure 2.

²⁶ This ensures consistency with our current Jeans setup.

²⁷ Defined by the most evident overlap between the three anisotropy curves and the dashed black line.

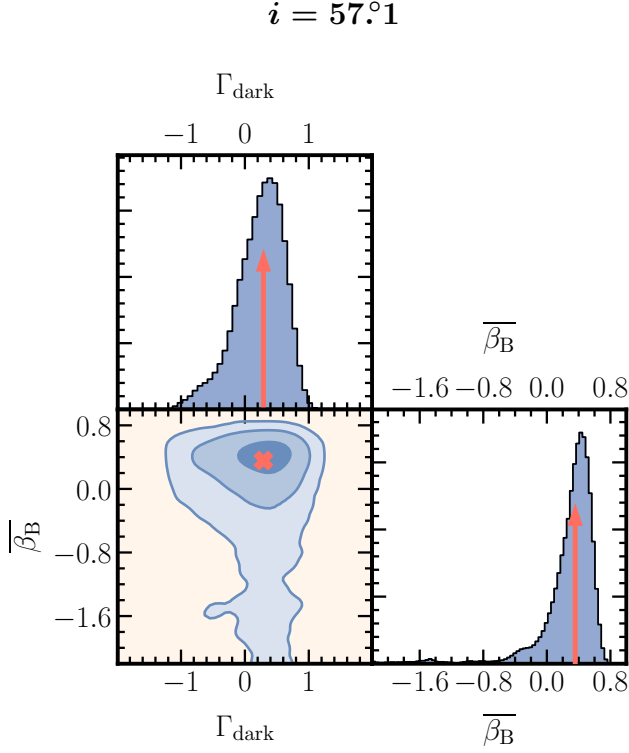


Figure 10. *Dark matter slope and velocity anisotropy:* Posterior probability distributions of Sculptor’s dark matter density slope, Γ_{dark} , averaged over the range where we have proper motion data, and the globally-averaged β_B velocity anisotropy (see Eq. [5]). These results correspond to a fiducial inclination of $57^\circ.1$, as argued in Section 4.2. Curves are lightly smoothed for simple visualization purposes. The values highlighted correspond to the median estimates (arrows, and cross).

Figure 7 illustrates the goodness-of-fit of the radial kinematic profiles from our Jeans models. Black points denote binned data: LOS kinematics on the left – annularly-averaged velocity dispersion (top) and major-axis rotation (bottom); and PM kinematics on the right – velocity dispersions in the radial (top) and tangential (bottom) directions. The solid black lines show the median model, while shaded regions represent MCMC percentiles, using the same fiducial inclination of $57^\circ.1$ to convert PMs to physical velocities. Model curves are interpolated over projected radius R for display, although they also vary with projected angle. The model provides a satisfactory overall agreement, consistent with fits at other inclinations.

4.3. Inferred Quantities

Degeneracies between inclination and parameters such as the DM inner slope and the velocity anisotropy profile render the inclination-averaged estimates of these quantities inconclusive, spanning a range of scenarios con-

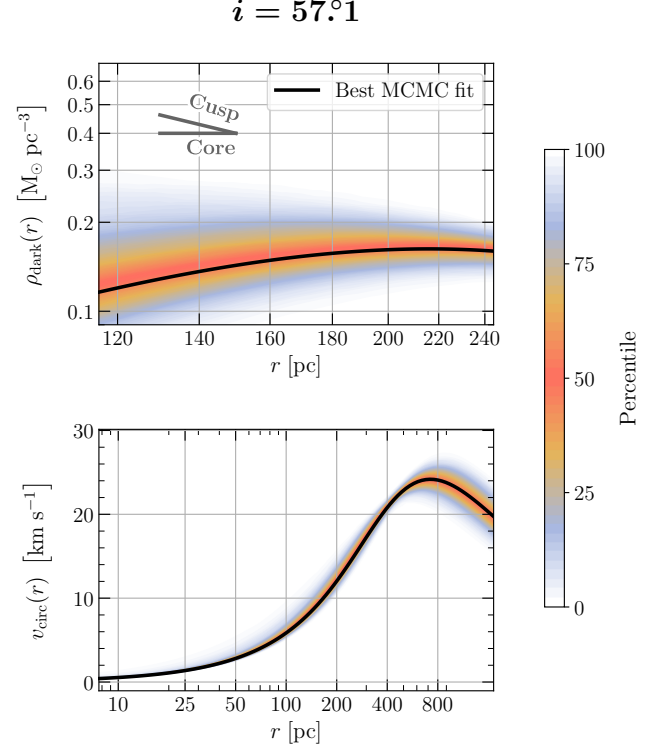


Figure 11. *Dark matter density and circular velocity:* The upper panel shows the 3D dark matter density profile within the radial range constrained by three-dimensional velocity data, with reference slopes for typical core and cusp profiles. The lower panel displays the corresponding circular velocity profile across the full radial extent of the data. Solid black lines indicate the median solution, while shaded colors represent percentiles of the MCMC chain. This result corresponds to a fiducial inclination of $57^\circ.1$, as argued in Section 4.2. The distance inferred for this inclination was used to convert angular to physical scales.

sistent with various cosmological models and DM candidates. However, incorporating higher-order moments, as outlined in Section 4.1.1, allows us to favor more flattened or less inclined configurations in the Jeans modeling. In this context, confidence in shallower DM slopes becomes notable: for our fiducial inclination of $i = 57^\circ.1$, we rule out $\Gamma_{\text{dark}} \leq -1$ at 99.8% confidence, while the inferred velocity anisotropy is mildly radial but still statistically consistent with isotropy. These trends are clearly reflected in the corner plots shown in Figure 10. Respectively, the confidence in such general patterns decreases or increases for more or less inclined systems.

The same trend is illustrated in the upper panel of Figure 11. Over the radial range spanned by the 3D-velocity data (i.e. the limits of the respective x axis) for the $i = 57^\circ.1$ model, the DM density profile clearly favors a shallow inner slope. As noted earlier, edge-on configurations yield more cuspy profiles, though they

are disfavored due to the higher LOS velocity kurtosis in the data. The same figure also presents Sculptor’s circular velocity profile for the fiducial inclination. Here, the velocity peaks at $\max(v_{\text{circ}}) = 24.18^{+1.29}_{-1.19} \text{ km s}^{-1}$, followed by a decline within the data extent – a feature not captured for Draco in Paper I, and in good agreement with the similarly non-spherical analysis of Hayashi et al. (2020, figure 9).

The DM mass enclosed within the data extent for the inclination-averaged fit – similar to values at other inclinations – is $M_{\text{dark}}^{R_{\text{max}}} = 1.39^{+0.68}_{-0.58} \times 10^8 M_{\odot}$, with an extrapolated total mass of $M_{\text{dark}}^{\text{total}} = 1.58^{+1.01}_{-0.62} \times 10^8 M_{\odot}$. This is far below the $\sim 10^{10} M_{\odot}$ inferred by Errani, Peñarrubia, & Walker (2018) for cored profiles, together with their $r_{\text{max}} \sim 10 \text{ kpc}$ and $v_{\text{max}} \sim 65 \text{ km s}^{-1}$. The difference is likely explained as follows: their method matches $M(< 1.8 R_{\text{h}})$ – a quantity consistent with ours²⁸ – to subhalos in the Aquarius simulations (Springel et al. 2008), but this does not guarantee agreement in the extrapolated outer halo. Because their approach links the halo outskirts directly to the mass within $1.8 R_{\text{h}}$, cusp and core models can produce very different M_{total} , r_{max} , and v_{max} . Our Jeans-based fits, in contrast, allow the outer profile to vary independently of correlations inherent to cosmological simulations, although our choice of a steeper outer slope²⁹ naturally yields lower total masses, even when matching at smaller radii. If Sculptor’s halo was once more massive and lost substantial DM to tidal interactions (see Section 5.1), this steep slope remains physically justified (Peñarrubia et al. 2010).

Beyond inclination-sensitive parameters, some constraints remain tight despite their correlations with inclination. This is the case for our inclination-averaged distance estimate, $D = 85.83^{+2.02}_{-1.91} \text{ kpc}$. This measurement is valuable in its own right, as dynamical distances provide an independent benchmark for stellar evolution models and parallax-based methods. The following sections assess the robustness of these results and their broader implications for cosmology and equilibrium-based mass modeling.

5. ROBUSTNESS OF MODELING RESULTS

5.1. The Effect of Tides

Perhaps the most fundamental assumption of our model is that the Sculptor dSph is in dynamical equilibrium. However, this galaxy orbits a significantly more

massive system (i.e. the Milky Way) and is therefore subject to tidal interactions that could perturb its equilibrium state. This possibility has been raised in previous studies to account for the inflated velocity dispersion profiles observed in dSphs, which appear larger than expected from their baryonic content alone (Klessen & Kroupa 1998; Hammer et al. 2018). Such arguments have even been used to question the necessity of DM in these systems, although the existence of satellites exhibiting high velocity dispersions while orbiting at relatively large pericentric distances (e.g. Li et al. 2021; Battaglia et al. 2022; Pace et al. 2022) remains a strong counterargument to this interpretation.

In our case, the total dark mass inferred for Sculptor is $1.58 \times 10^8 M_{\odot}$, nearly an order of magnitude lower than the $4.85 \times 10^9 M_{\odot}$ predicted by Λ CDM scaling relations for low-mass dwarfs (Read et al. 2017). This discrepancy could be somewhat accounted if a large fraction of Sculptor’s DM halo has been stripped by the Milky Way’s tidal field over its lifetime. Such a scenario is consistent with orbital reconstructions (e.g., Sohn et al. 2017), which indicate several close pericentric passages around the Milky Way, that would have favored substantial mass loss.

Sculptor’s dynamical stability under such conditions was examined by Iorio et al. (2019), who ran simulations to evaluate how tidal interactions might affect the system and the validity of equilibrium-based mass estimates. Even under extreme orbital scenarios permitted by current observed data, they found little evidence for significant tidal disturbance in the stellar distribution. While the DM halo may undergo stripping, the stars themselves remain largely unaffected, showing only gradual changes over time. In the last 2 Gyr, they found these variations to be minimal, well within a few percent. Such findings, alongside similar conclusions from more recent studies (e.g., Tchiorniy & Genina 2025), support the use of equilibrium-based models for estimating Sculptor’s inner mass profile.

5.2. Tests with mock data

As a final robustness check, we apply our modeling strategies to mock datasets to evaluate both their performance and the influence of key assumptions. We focus on two primary tests: First, we simulate a system that adheres to the assumptions of our modeling framework, and examine whether elements such as the use of Gaussian likelihoods for projected velocities or our data-cleaning procedures – particularly the local PM corrections applied to mitigate systematics – introduce significant biases in the inferred parameters. Second, we assess the impact of multiple kinematic populations

²⁸ Errani et al. (2018) predict $M(< 1.8 R_{\text{h}}) = 3.2 \pm 0.7 \times 10^7 M_{\odot}$, while our inclination averaged measurement is $M(< 1.8 R_{\text{h}}) = 5 \pm 2 \times 10^7 M_{\odot}$.

²⁹ $\beta = 5$ in the generalized $\alpha\beta\gamma$ model.

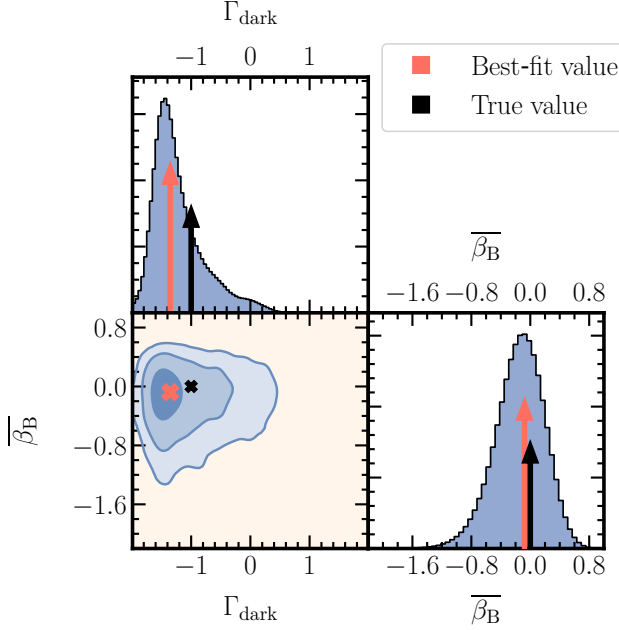


Figure 12. *Mock test #1:* Corner plot of the Jeans fit to a mock dataset generated with AGAMA, following the overall assumptions of our modeling, for a selection of most relevant parameters: the asymptotic inner slope of the DM profile over the range where 3D velocities are available, and the average velocity anisotropy $\overline{\beta}_B$ (Eq. 5). The black arrows and crosses (smaller) represent the true values used to construct the mock, while the larger red markers correspond to the best-fit values from our analysis. The blue posterior distributions are also shown. The close agreement between the estimates and true values indicates that our data handling – including the removal of streaming motions through local systematic error corrections – does not introduce significant biases, assuming the validity of our parametrization choices.

within Sculptor, despite our modeling being based on a single-component assumption.

To conduct these tests, we employ the distribution function-based code AGAMA (Vasiliev 2019) to generate spherical³⁰ stellar systems in equilibrium, given a potential and mass distribution. Each mock setup is described below, while the general procedure used to align the mocks with the observed data is detailed in Appendix A.

5.2.1. Data and Likelihood Handling

For the first test, we construct a rotating mock system consisting of an isotropic Plummer stellar component with the same total mass and scale radius as Sculptor (see Appendix A for details). The DM halo is modeled

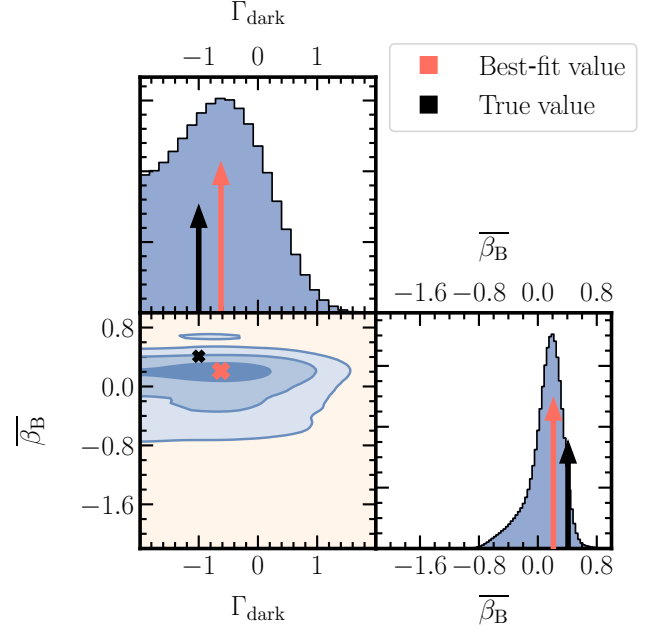


Figure 13. *Mock test #2:* Same as Figure 12, but using a mock dataset with two distinct kinematic populations (i.e., differing in both velocity anisotropy and density distribution). The average velocity anisotropy $\overline{\beta}_B$ (Eq. 5) remains relatively well constrained thanks to the 3D velocity data, while the Γ_{dark} parameter (Eq. 8) shows a mild loss in fitting performance, though still consistent within 1- σ uncertainties.

using a cuspy generalized Plummer profile (i.e., $\gamma = -1$), with the total mass and scale radius set according to the expectations from Λ CDM cosmology, as outlined in Section 3.1.1.

By comparing our fits to this simulated data to the true input values, we can assess the impact of our local PM corrections to eliminate *HST* systematic effects, as well as evaluate the performance of our fitting strategy. Figure 12 shows this comparison for a selection of the most relevant fit parameters: the slope of the DM profile over the region where 3D velocities are available, Γ_{dark} , and the globally-averaged $\overline{\beta}_B$ (cf. Eq. 5). The close agreement between the smaller black markers (true values) and the larger red markers (estimated values) highlights the proper handling of the data and demonstrates satisfactory convergence of our fit, assuming the parametrizations are correct. Additionally, the posterior distributions in blue exhibit similar widths to those obtained from fitting the true data, which further supports the reliability of our error bars presented in Table 2.

5.2.2. Distinct kinematic populations

One of the key outcomes of spectroscopic campaigns targeting dSphs, with Sculptor frequently serving as a

³⁰ At present, AGAMA does not support fully axisymmetric distributions with a given anisotropy and density profile, as would be ideal for comparison with the observed data.

benchmark system, has been the identification of at least two distinct chemo-dynamical populations (e.g. Tolstoy et al. 2004). These subpopulations have proven instrumental in mitigating degeneracies inherent to mass modeling based solely on LOS velocity measurements (e.g. Walker & Peñarrubia 2011). More recently, expanded observational efforts (Tolstoy et al. 2023; Barbosa et al. 2025) have substantially advanced the characterization of Sculptor’s internal kinematics, yielding improved constraints on the spatial distributions, membership probabilities, and LOS velocity dispersion profiles of its distinct stellar populations (e.g. Arroyo-Polonio et al. 2024).

This naturally raises the question of whether modeling the system as a single dynamical component introduces bias – particularly in the estimation of key parameters such as Γ_{dark} and the mean β_B for the data. To assess the potential impact of multiple stellar populations, we simulate a composite system comprising metal-poor and metal-rich components. These components are designed to approximate the spatial and kinematic structure inferred by Arroyo-Polonio et al. (2025) for Sculptor, as illustrated in their figure 1, but without rotation, as not to mix different test diagnostics. To implement this, we extracted the relevant data from that figure using online plot digitization tools,³¹ and fitted each population: we used a Plummer profile for the surface density and constant velocity anisotropy model for their inferred β_B .³² We then assigned tracer counts based on the normalization of each fitted density profile.

Figure 13 presents the results of our fits to this chemo-dynamically distinct mock dataset, focusing on the same key parameters evaluated in the previous test. Overall, we find that the estimates remain consistent within $1\text{-}\sigma$ uncertainties, albeit with slightly reduced performance compared to the single-population case. Notably, the posterior distribution of the Γ_{dark} parameter exhibits a different shape and central value, suggesting that neglecting multiple populations may slightly inflate the formal uncertainties. This behavior implies a potential bias in precision and accuracy. In summary, while the simplified single-population modeling does not introduce substantial bias in the recovery of the DM density profile, it is not entirely neutral and may slightly favor

shallower inner slopes relative to Sculptor’s true underlying profile. Meanwhile, the average velocity anisotropy remains relatively well constrained, benefiting from the full 3D velocity information.

6. DISCUSSION

6.1. Implications for mass modeling

Nearby dSphs provide a rare opportunity to test small-scale predictions of cosmological models using resolved stellar kinematics. This has driven extensive LOS velocity surveys with ground-based telescopes (e.g., Tolstoy et al. 2004; Walker et al. 2007; Gilmore et al. 2022), aimed at constraining the underlying DM distributions. Many mass-modeling studies, however, have relied on simplifying assumptions: most notably, spherical symmetry (e.g., Battaglia et al. 2008; Walker & Peñarrubia 2011; Read et al. 2018; Arroyo-Polonio et al. 2025), despite clear observational evidence that dSphs are flattened systems (e.g., Muñoz et al. 2018). Even with growing access to more complex PM data (e.g., Massari et al. 2017, 2020), few works have incorporated intrinsic geometry into their models (see Hayashi et al. 2020 and Pace et al. 2020).

Our results, consistent with Paper I, demonstrate that accounting for dSph flattening significantly alters the inferred DM density profile and stellar orbital structure. While Paper I emphasized how the projected velocity anisotropy varies with position angle, potentially biasing DM slope estimates under spherical symmetry,³³ our current analysis highlights a strong dependence on the galaxy’s inclination. This introduces a key degeneracy overlooked by spherical, non-rotating models. As shown in Table 2, several modeled parameters shift with inclination, in some cases beyond formal uncertainties.

These findings support the case for more flexible modeling frameworks, even those possibly including non-spherical or triaxial DM halos and baryonic content. Yet, such approaches remain difficult in practice due to the lack of independent constraints on 3D shapes for individual dSphs. Axisymmetric models offer a pragmatic middle ground, requiring only projected flattening and inclination, with the former already well measured. Independent inclination constraints may soon be accessible through future *Gaia* data releases, which will deliver higher precision maps of mean PM, hopefully with higher signal than *Gaia*’s systematic uncertainties. Combining these with LOS velocity data via established formalisms (e.g., Evans & de Zeeuw 1994;

³¹ Specifically, <https://web.eecs.utk.edu/~dcostine/personal/PowerDeviceLib/DigiTest/index.html>.

³² As discussed in Section 3.1.1, separate tests showed that assuming a radially varying anisotropy did not significantly alter the results presented in Table 2, thereby justifying the simpler assumption of a constant value per population. Moreover, the large β_B uncertainties in figure 1 of Arroyo-Polonio et al. (2025) are statistically consistent with this simplified treatment.

³³ In spherical models, observables are assumed to be identical at a given radius regardless of position angle.

Bianchini et al. 2018) may finally enable robust, model-independent estimates of dSph inclinations.

Another important complexity – often not explicitly modeled, including in this study – is the presence of multiple chemically-distinct stellar populations within dSphs. Many systems are known to host at least two such populations, typically metal-poor and metal-rich, which exhibit different LOS velocity dispersions (e.g., Pace et al. 2020; Arroyo-Polonio et al. 2024). Whether these populations require separate anisotropy prescriptions in Jeans-based modeling remains an open question, with only a limited number of systems studied in detail (e.g., Arroyo-Polonio et al. 2025). In the specific case of Sculptor, our mock data tests suggest that treating its stars as a single dynamical component does not lead to significant bias in the recovered DM density profile, though it may introduce a modest loss of accuracy within the formal $1\text{-}\sigma$ uncertainty range.³⁴

This underscores the advantages of better associating PMs with distinct chemical populations to fully exploit 3D kinematics. Progress will depend on joint astrometric and spectroscopic observations, especially at faint magnitudes where most dSph stars lie and where facilities like *HST*, *JWST*, *Euclid* (e.g. Libralato et al. 2024) and the upcoming *Nancy Grace Roman Space Telescope* will be crucial.

6.2. Implications for the nature of dark matter

As discussed in Sections 4.1 and 4.3, significant degeneracies arise due to Sculptor’s unknown inclination, preventing firm constraints on the nature of DM across the full range of tested configurations. These limitations stem from both the data, such as the lack of odd PM moments by design, and our modeling approach, which in the Jeans formalism does not account for velocity moments beyond second order. However, as shown in Section 4.1.1 and in Section 5.4 of Paper I, higher-order moments of the LOS velocities provide additional information on velocity anisotropy and the galaxy’s shape, helping to alleviate these degeneracies (e.g. Read & Steger 2017; Read et al. 2018). While our analysis does not yield a precise estimate of Sculptor’s inclination, comparisons with SCALEFREE models from de Bruijne et al. (1996) suggest that Sculptor likely favors a more flattened and less inclined configuration, deviating from an edge-on geometry.

At low inclination, we find that the DM slope within the PM-covered region is constrained toward shallower

values, deviating from the cuspy profiles predicted by Λ CDM DM-only simulations (Navarro et al. 1997). This result supports previous findings that favor core-like DM profiles in dSphs, based on stellar kinematics (e.g. Battaglia et al. 2008; Walker & Peñarrubia 2011; Zhu et al. 2016; Amorisco & Evans 2012; Brownsberger & Randall 2021; Arroyo-Polonio et al. 2025) and HI rotation curves (e.g. Moore 1994; Flores & Primack 1994; Burkert 1995). Within Λ CDM, the most common explanation involves the influence of baryonic processes, which can transform central cusps into cores by redistributing mass and energy via supernova feedback (Read & Gilmore 2005; Pontzen & Governato 2012; Brooks & Zolotov 2014) or bursts of star formation (Read et al. 2018). Indeed, Fitts et al. (2017) identify a threshold around $M_\star \approx 2 \times 10^6 M_\odot$, above which these effects become efficient.

The comparison of total stellar masses between Draco ($4.7 \times 10^5 M_\odot$, Martin et al. 2008, Paper I), where we found a clear preference for a cusp, and Sculptor ($8.08 \times 10^6 M_\odot$, de Boer et al. 2012, this work), where our analyses seem to favor a core, qualitatively supports this picture and presents no direct challenge to Λ CDM. Nonetheless, underlying quantitative details remain uncertain. For instance, is there a predictable analytical or empirical link between the degree of DM slope flattening (i.e., the value of γ_{dark}) and a galaxy’s baryonic content? How does the host halo mass, fixed at $M_{\text{halo}} \approx 10^{10} M_\odot$ in Fitts et al. (2017), modulate this process? And how long would it take for a system like Sculptor to regenerate a cuspy density profile from the apparent present-day core? (e.g. Laporte & Penarrubia 2015) These questions point to the need for more nuanced exploration of stellar feedback in cosmological simulations to reproduce the configurations favored by our fits. In parallel, our results serve as valuable observational constraints for testing both Λ CDM and alternative models in which core formation arises naturally, such as self-interacting DM (SIDM, e.g. Nadler, Yang, & Yu 2023) with larger cross sections or Fuzzy DM with specific particle mass ranges (Luu et al. 2025).

7. CONCLUSIONS

We present a new proper motion catalog for the Sculptor dwarf spheroidal galaxy, comprising 119 stars with proper motion uncertainties smaller than the galaxy’s intrinsic velocity dispersion (i.e. $\sim 10 \text{ km s}^{-1}$) – making it the most precise proper motion dataset compiled for this system to date. We also combined line-of-sight velocities from multiple literature sources, resulting in a sample of 1,760 stars with similarly low velocity uncertainties. Using this state-of-the-art public

³⁴ Besides, the locations of the 16th and 84th percentiles may change, while their relative distance to each other seems somewhat the same as the one from the single population test.

dataset,³⁵ we conducted axisymmetric Jeans-based mass and anisotropy modeling, complemented by robustness tests involving higher-order velocity moments and mock datasets. Below, we summarize the main conclusions of this work.

- We present updated estimates for Sculptor’s center, ellipticity, position angle, and scale radius, based on fits to stellar counts from *Gaia* EDR3 (Table 1).
- We confirm mild oblate rotation, with major-axis amplitudes reaching up to $\sim 2 \text{ km s}^{-1}$ beyond 20'0 from the galaxy center, consistent with recent line-of-sight based findings (Arroyo-Polonio et al. 2024).
- We demonstrate that unresolved binaries have a negligible effect on the line-of-sight velocity dispersion and thus do not significantly impact the dynamical modeling.
- From proper motions measured in our *HST* fields along the projected minor axis, we find average observed velocity dispersion ratios of $\langle \sigma_{\text{POS}t} \rangle / \langle \sigma_{\text{POS}r} \rangle = 1.19 \pm 0.19$ and $\langle \sigma_{\text{LOS}} \rangle / \langle \sigma_{\text{POS}} \rangle = 0.93 \pm 0.08$, where σ_{POS} is the average dispersion across both proper motion directions. The first ratio is independent of distance, while the second scales inversely with it.³⁶
- We perform tests with mock datasets constructed using AGAMA to confirm that our current treatment of *HST* proper motion systematics does not introduce significant biases in the fitted parameters of our Jeans modeling. Additionally, for the specific case of Sculptor, we show that modeling its stellar component as a single dynamical population does not significantly bias the recovered DM density profile, though it may introduce a modest reduction in precision and accuracy within the formal 1- σ uncertainty range.
- Our non-spherical modeling reveals a significant degeneracy tied to the unknown inclination of the galaxy – an effect missed under spherical symmetry assumptions. This degeneracy allows acceptable fits across a wide range of dark matter profiles, from cuspy to cored and even centrally-decreasing density configurations. While we do not directly constrain the inclination, higher-order

line-of-sight velocity moments provide useful limits, and comparisons with SCALEFREE models from de Bruijne et al. (1996) favor highly flattened (i.e., less inclined) configurations.

- For a representative low inclination of $i = 57^\circ$, near the median of the inferred inclination PDF (Figure 2), we find, alongside well-constrained radial velocity anisotropy, a dark matter density slope of $\Gamma_{\text{dark}} = 0.29^{+0.31}_{-0.41}$ within the radial extent of our 3D velocity data, ruling out $\Gamma_{\text{dark}} \leq -1$ at 99.8% confidence.³⁷ This confidence level increases with lower inclinations and decreases for close to edge-on configurations. At the same inclination, we infer a maximum circular velocity of $\max(v_{\text{circ}}) = 24.18^{+1.29}_{-1.19} \text{ km s}^{-1}$.
- At lower inclinations, our results qualitatively agree with Λ CDM predictions in which feedback in higher-mass dwarf galaxies produces shallower dark matter profiles (Fitts et al. 2017). These models predict a transition from cusp to core at $M_\star \approx 2 \times 10^6 \text{ M}_\odot$, while Sculptor’s total stellar mass is $8.08 \times 10^6 \text{ M}_\odot$ (de Boer et al. 2012). Likewise, alternative DM models such as SIDM and Fuzzy DM also predict core formation for specific ranges of cross sections and particle masses, respectively, making our measurements a useful means of narrowing these parameter spaces.
- Averaged over all inclinations, we estimate an enclosed mass within the radial extent of our data of $M_{\text{dark}}^{R_{\text{max}}} = 1.39^{+0.68}_{-0.58} \times 10^8 \text{ M}_\odot$, and a total dark matter mass of $M_{\text{dark}}^{\text{total}} = 1.58^{+1.01}_{-0.62} \times 10^8 \text{ M}_\odot$. The modest increase beyond R_{max} reflects our choice of a steep outer halo slope ($\beta = 5$), consistent with expectations for tidally affected satellites (Peñarrubia et al. 2010). We also constrain a dynamical distance of $D = 85.83^{+2.02}_{-1.91} \text{ kpc}$.

Following the conclusions from the first paper in this series (Paper I), we reaffirm the growing potential for a deeper understanding of dwarf spheroidal galaxy internal kinematics. This progress relies on assembling long time-baseline proper motion datasets with the most precise astrometric facilities, such as *HST*, *JWST*, and *Gaia*, and on the development of future missions like *Roman*. Ongoing work includes observations of additional systems (e.g. Vitral et al. 2023b) and the refinement

³⁵ We will make the data public upon paper acceptance.

³⁶ We assumed here $D = 85.83 \text{ kpc}$.

³⁷ An asymptotic dark matter density slope of -1 represents the classic inference from dark matter only Λ CDM simulations (Navarro et al. 1997)

of *HST*-based measurements using *JWST* (e.g. van der Marel et al. 2023; Bennet et al. 2025a,b).³⁸ With such data, significant advances in galactic dynamics and dark matter studies are within reach.

8. ACKNOWLEDGMENTS

Eduardo Vitral acknowledges funding from the Royal Society, under the Newton International Fellowship programme (NIF\R1\241973). Support for this work was provided by NASA through grants for programs GO-12966 and GO-16737 from the Space Telescope Science Institute (STScI), which is operated by the Association of Universities for Research in Astronomy (AURA), Inc., under NASA contract NAS5-26555, and through funding to the *JWST* Telescope Scientist Team (PI: M. Mountain) through grant 80NSSC20K0586. We thank Justin Read and Thomas de Boer, for sharing the algorithms used in Read et al. (2017) and de Boer et al. (2012), respectively.

The Digitized Sky Surveys were produced at the Space Telescope Science Institute under U.S. Government grant NAG W-2166. The images of these surveys are based on photographic data obtained using the Oschin Schmidt Telescope on Palomar Mountain and the UK Schmidt Telescope. The plates were processed into the present compressed digital form with the permission of these institutions.

This work has made use of data from the European Space Agency (ESA) mission *Gaia* (<https://www.cosmos.esa.int/gaia>), processed by the *Gaia* Data Pro-

cessing and Analysis Consortium (DPAC, <https://www.cosmos.esa.int/web/gaia/dpac/consortium>). Funding for the DPAC has been provided by national institutions, in particular the institutions participating in the *Gaia* Multilateral Agreement.

This project is part of the HSTPROMO (High-resolution Space Telescope PROper MOtion) Collaboration (<https://www.stsci.edu/~marel/hstpromo.html>), a set of projects aimed at improving our dynamical understanding of stars, clusters, and galaxies in the nearby Universe through measurement and interpretation of PMs from *HST*, *Gaia*, *JWST*, and other space observatories. We thank the collaboration members for the sharing of their ideas and software.

Data availability: The data that we used to construct proper motions were obtained from the Mikulski Archive for Space Telescopes (MAST) at the Space Telescope Science Institute. See Appendix B for the data products of this work.

Facilities: HST; Gaia; Magellan:Clay; VLT:Kueyen.

Software: PYTHON (Van Rossum & Drake 2009), BALROGO (Vital 2021), JAMPY (Cappellari 2020), EMCEE (Foreman-Mackey et al. 2013), SCIPY (Jones et al. 2001–), NUMPY (van der Walt et al. 2011), MATPLOTLIB (Hunter 2007), AGAMA (Vasiliev 2019), APLPY (Robitaille & Bressert 2012), SCALEFREE (de Bruijne et al. 1996), and the Scientific color maps from Crameri, Shephard, & Heron (2020).

REFERENCES

- Amorisco, N. C., & Evans, N. W. 2012, MNRAS, 419, 184, doi: [10.1111/j.1365-2966.2011.19684.x](https://doi.org/10.1111/j.1365-2966.2011.19684.x)
- Anderson, J. 2022, One-Pass HST Photometry with hst1pass, Instrument Science Report ACS 2022-02
- Anderson, J., Bedin, L. R., Piotto, G., Yadav, R. S., & Bellini, A. 2006, A&A, 454, 1029, doi: [10.1051/0004-6361:20065004](https://doi.org/10.1051/0004-6361:20065004)
- Arroyo-Polonio, J. M., Battaglia, G., Thomas, G. F., et al. 2023, A&A, 677, A95, doi: [10.1051/0004-6361/202346843](https://doi.org/10.1051/0004-6361/202346843)
- . 2024, A&A, 692, A195, doi: [10.1051/0004-6361/202451102](https://doi.org/10.1051/0004-6361/202451102)
- Arroyo-Polonio, J. M., Pascale, R., Battaglia, G., et al. 2025, A&A, 699, A347, doi: [10.1051/0004-6361/202554826](https://doi.org/10.1051/0004-6361/202554826)
- Bacon, R., Simien, F., & Monnet, G. 1983, A&A, 128, 405
- Barbosa, F. O., Chiti, A., Limberg, G., et al. 2025, arXiv e-prints, arXiv:2504.03593, doi: [10.48550/arXiv.2504.03593](https://doi.org/10.48550/arXiv.2504.03593)
- Battaglia, G., Helmi, A., Tolstoy, E., et al. 2008, ApJL, 681, L13, doi: [10.1086/590179](https://doi.org/10.1086/590179)
- Battaglia, G., Taibi, S., Thomas, G. F., & Fritz, T. K. 2022, A&A, 657, A54, doi: [10.1051/0004-6361/202141528](https://doi.org/10.1051/0004-6361/202141528)
- Beers, T. C., Flynn, K., & Gebhardt, K. 1990, AJ, 100, 32
- Bellini, A., Libralato, M., Bedin, L. R., et al. 2018, ApJ, 853, 86, doi: [10.3847/1538-4357/aaa3ec](https://doi.org/10.3847/1538-4357/aaa3ec)
- Bennet, P., Bellini, A., Fardal, M., et al. 2025a, Enabling cross instrument proper motions with Draco dSph and NGC 2419, HST Proposal. Cycle 32, ID. #17926

³⁸ These proposals can be retrieved in the following links:
<https://ui.adsabs.harvard.edu/abs/2023hst..prop17434V/>.
<https://ui.adsabs.harvard.edu/abs/2023jwst.prop.4513V/>.
<https://ui.adsabs.harvard.edu/abs/2025hst..prop17926B/>.
<https://ui.adsabs.harvard.edu/abs/2025jwst.prop.9225B/>.

- . 2025b, Enabling cross instrument proper motions with Draco dSph and NGC 2419, JWST Proposal. Cycle 3, ID. #9225
- Bertone, G., Hooper, D., & Silk, J. 2005, *PhR*, 405, 279
- Bianchini, P., van der Marel, R. P., del Pino, A., et al. 2018, *MNRAS*, 481, 2125, doi: [10.1093/mnras/sty2365](https://doi.org/10.1093/mnras/sty2365)
- Binney, J. 1980, *MNRAS*, 190, 873
- Binney, J., & Mamon, G. A. 1982, *MNRAS*, 200, 361, doi: [10.1093/mnras/200.2.361](https://doi.org/10.1093/mnras/200.2.361)
- Boldrini, P. 2021, *Galaxies*, 10, 5, doi: [10.3390/galaxies10010005](https://doi.org/10.3390/galaxies10010005)
- Brooks, A. M., & Zolotov, A. 2014, *ApJ*, 786, 87, doi: [10.1088/0004-637X/786/2/87](https://doi.org/10.1088/0004-637X/786/2/87)
- Brownsberger, S. R., & Randall, L. 2021, *MNRAS*, 501, 2332, doi: [10.1093/mnras/staa3719](https://doi.org/10.1093/mnras/staa3719)
- Bullock, J. S., & Boylan-Kolchin, M. 2017, *ARA&A*, 55, 343, doi: [10.1146/annurev-astro-091916-055313](https://doi.org/10.1146/annurev-astro-091916-055313)
- Burkert, A. 1995, *ApJL*, 447, L25
- Cappellari, M. 2020, *MNRAS*, 494, 4819, doi: [10.1093/mnras/staa959](https://doi.org/10.1093/mnras/staa959)
- Chanamé, J., Kleyna, J., & van der Marel, R. 2008, *ApJ*, 682, 841, doi: [10.1086/589429](https://doi.org/10.1086/589429)
- Collins, M. L. M., & Read, J. I. 2022, *Nature Astronomy*, 6, 647, doi: [10.1038/s41550-022-01657-4](https://doi.org/10.1038/s41550-022-01657-4)
- Crameri, F., Shephard, G. E., & Heron, P. J. 2020, *Nature Communications*, 11, 5444, doi: [10.1038/s41467-020-19160-7](https://doi.org/10.1038/s41467-020-19160-7)
- de Boer, T. J. L., Tolstoy, E., Hill, V., et al. 2012, *A&A*, 539, A103, doi: [10.1051/0004-6361/201118378](https://doi.org/10.1051/0004-6361/201118378)
- de Bruijne, J. H. J., van der Marel, R. P., & de Zeeuw, P. T. 1996, *MNRAS*, 282, 909, doi: [10.1093/mnras/282.3.909](https://doi.org/10.1093/mnras/282.3.909)
- del Pino, A., Libralato, M., van der Marel, R. P., et al. 2022, *ApJ*, 933, 76, doi: [10.3847/1538-4357/ac70cf](https://doi.org/10.3847/1538-4357/ac70cf)
- Dutton, A. A., & Macciò, A. V. 2014, *MNRAS*, 441, 3359, doi: [10.1093/mnras/stu742](https://doi.org/10.1093/mnras/stu742)
- Errani, R., Peñarrubia, J., & Walker, M. G. 2018, *MNRAS*, 481, 5073, doi: [10.1093/mnras/sty2505](https://doi.org/10.1093/mnras/sty2505)
- Evans, N. W., & de Zeeuw, P. T. 1994, *MNRAS*, 271, 202, doi: [10.1093/mnras/271.1.202](https://doi.org/10.1093/mnras/271.1.202)
- Fitts, A., Boylan-Kolchin, M., Elbert, O. D., et al. 2017, *MNRAS*, 471, 3547, doi: [10.1093/mnras/stx1757](https://doi.org/10.1093/mnras/stx1757)
- Flores, R. A., & Primack, J. R. 1994, *ApJL*, 427, L1, doi: [10.1086/187350](https://doi.org/10.1086/187350)
- Foreman-Mackey, D., Hogg, D. W., Lang, D., & Goodman, J. 2013, *PASP*, 125, 306, doi: [10.1086/670067](https://doi.org/10.1086/670067)
- Gaia Collaboration, Helmi, A., van Leeuwen, F., et al. 2018, *A&A*, 616, A12, doi: [10.1051/0004-6361/201832698](https://doi.org/10.1051/0004-6361/201832698)
- Gilmore, G., Randich, S., Worley, C. C., et al. 2022, *A&A*, 666, A120, doi: [10.1051/0004-6361/202243134](https://doi.org/10.1051/0004-6361/202243134)
- Goldstein, I. S., & Strigari, L. E. 2025, *MNRAS*, 541, 1016, doi: [10.1093/mnras/staf1026](https://doi.org/10.1093/mnras/staf1026)
- Górski, M., Pietrzyński, G., & Gieren, W. 2011, *AJ*, 141, 194, doi: [10.1088/0004-6256/141/6/194](https://doi.org/10.1088/0004-6256/141/6/194)
- Grebel, E. K. 2009, in *IAU Symposium*, Vol. 254, The Galaxy Disk in Cosmological Context, ed. J. Andersen, Nordströara, B. m, & J. Bland-Hawthorn, 49–60, doi: [10.1017/S1743921308027385](https://doi.org/10.1017/S1743921308027385)
- Hammer, F., Yang, Y., Arenou, F., et al. 2018, *ApJ*, 860, 76, doi: [10.3847/1538-4357/aac3da](https://doi.org/10.3847/1538-4357/aac3da)
- Hayashi, K., Chiba, M., & Ishiyama, T. 2020, *ApJ*, 904, 45, doi: [10.3847/1538-4357/abbe0a](https://doi.org/10.3847/1538-4357/abbe0a)
- Hunter, J. D. 2007, *Computing in Science & Engineering*, 9, 90, doi: [10.1109/MCSE.2007.55](https://doi.org/10.1109/MCSE.2007.55)
- Iorio, G., Nipoti, C., Battaglia, G., & Sollima, A. 2019, *MNRAS*, 487, 5692, doi: [10.1093/mnras/stz1342](https://doi.org/10.1093/mnras/stz1342)
- Jones, E., Oliphant, T., Peterson, P., et al. 2001–, *SciPy: Open source scientific tools for Python*. <http://www.scipy.org/>
- Klessen, R. S., & Kroupa, P. 1998, *ApJ*, 498, 143, doi: [10.1086/305540](https://doi.org/10.1086/305540)
- Kozhurina-Platais, V., Borncamp, D., Anderson, J., Grogin, N., & Hack, M. 2015, *ACS/WFC Revised Geometric Distortion for DrizzlePac*, Instrument Science Report ACS/WFC 2015-06, 47 pages
- Lambas, D. G., Maddox, S. J., & Loveday, J. 1992, *MNRAS*, 258, 404, doi: [10.1093/mnras/258.2.404](https://doi.org/10.1093/mnras/258.2.404)
- Laporte, C. F. P., & Penarrubia, J. 2015, *MNRAS*, 449, L90, doi: [10.1093/mnrasl/slv008](https://doi.org/10.1093/mnrasl/slv008)
- Li, T. S., Koposov, S. E., Erkal, D., et al. 2021, *ApJ*, 911, 149, doi: [10.3847/1538-4357/abeb18](https://doi.org/10.3847/1538-4357/abeb18)
- Libralato, M., Bellini, A., Bedin, L. R., et al. 2014, *A&A*, 563, A80, doi: [10.1051/0004-6361/201322059](https://doi.org/10.1051/0004-6361/201322059)
- Libralato, M., Bellini, A., van der Marel, R. P., et al. 2018, *ApJ*, 861, 99, doi: [10.3847/1538-4357/aac6c0](https://doi.org/10.3847/1538-4357/aac6c0)
- . 2023, *ApJ*, 950, 101, doi: [10.3847/1538-4357/acd04f](https://doi.org/10.3847/1538-4357/acd04f)
- Libralato, M., Bedin, L. R., Griggio, M., et al. 2024, *A&A*, 692, A96, doi: [10.1051/0004-6361/202452295](https://doi.org/10.1051/0004-6361/202452295)
- Luu, H. N., Mocz, P., Vogelsberger, M., et al. 2025, *PhRvD*, 111, L121302, doi: [10.1103/w9j1-k7b3](https://doi.org/10.1103/w9j1-k7b3)
- Martin, N. F., de Jong, J. T. A., & Rix, H.-W. 2008, *ApJ*, 684, 1075, doi: [10.1086/590336](https://doi.org/10.1086/590336)
- Massari, D., Helmi, A., Mucciarelli, A., et al. 2020, *A&A*, 633, A36, doi: [10.1051/0004-6361/201935613](https://doi.org/10.1051/0004-6361/201935613)
- Massari, D., Posti, L., Helmi, A., Fiorentino, G., & Tolstoy, E. 2017, *A&A*, 598, L9, doi: [10.1051/0004-6361/201630174](https://doi.org/10.1051/0004-6361/201630174)
- McConnachie, A. W. 2012, *AJ*, 144, 4, doi: [10.1088/0004-6256/144/1/4](https://doi.org/10.1088/0004-6256/144/1/4)

- McKinnon, K. A., del Pino, A., Rockosi, C. M., et al. 2024, *ApJ*, 972, 150, doi: [10.3847/1538-4357/ad5834](https://doi.org/10.3847/1538-4357/ad5834)
- Merritt, D. 1985, *ApJ*, 289, 18
- . 1987, *ApJ*, 313, 121
- Minor, Q. E., Martinez, G., Bullock, J., Kaplinghat, M., & Trainor, R. 2010, *ApJ*, 721, 1142, doi: [10.1088/0004-637X/721/2/1142](https://doi.org/10.1088/0004-637X/721/2/1142)
- Moore, B. 1994, *Nature*, 370, 629+
- Muñoz, R. R., Côté, P., Santana, F. A., et al. 2018, *ApJ*, 860, 66, doi: [10.3847/1538-4357/aac16b](https://doi.org/10.3847/1538-4357/aac16b)
- Nadler, E. O., Yang, D., & Yu, H.-B. 2023, *ApJL*, 958, L39, doi: [10.3847/2041-8213/ad0e09](https://doi.org/10.3847/2041-8213/ad0e09)
- Navarro, J. F., Frenk, C. S., & White, S. D. M. 1997, *ApJ*, 490, 493, doi: [10.1086/304888](https://doi.org/10.1086/304888)
- Osipkov, L. P. 1979, *Soviet Astronomy Letters*, 5, 42
- Pace, A. B. 2024, arXiv e-prints, arXiv:2411.07424, doi: [10.48550/arXiv.2411.07424](https://doi.org/10.48550/arXiv.2411.07424)
- Pace, A. B., Erkal, D., & Li, T. S. 2022, *ApJ*, 940, 136, doi: [10.3847/1538-4357/ac997b](https://doi.org/10.3847/1538-4357/ac997b)
- Pace, A. B., Kaplinghat, M., Kirby, E., et al. 2020, *MNRAS*, 495, 3022, doi: [10.1093/mnras/staa1419](https://doi.org/10.1093/mnras/staa1419)
- Peñarrubia, J., Benson, A. J., Walker, M. G., et al. 2010, *MNRAS*, 406, 1290, doi: [10.1111/j.1365-2966.2010.16762.x](https://doi.org/10.1111/j.1365-2966.2010.16762.x)
- Pianta, C., Capuzzo-Dolcetta, R., & Carraro, G. 2022, *ApJ*, 939, 3, doi: [10.3847/1538-4357/ac9303](https://doi.org/10.3847/1538-4357/ac9303)
- Pietrzyński, G., Gieren, W., Szweczyk, O., et al. 2008, *AJ*, 135, 1993, doi: [10.1088/0004-6256/135/6/1993](https://doi.org/10.1088/0004-6256/135/6/1993)
- Plummer, H. C. 1911, *MNRAS*, 71, 460
- Pontzen, A., & Governato, F. 2012, *MNRAS*, 421, 3464, doi: [10.1111/j.1365-2966.2012.20571.x](https://doi.org/10.1111/j.1365-2966.2012.20571.x)
- Pryor, C., & Kormendy, J. 1990, *AJ*, 100, 127, doi: [10.1086/115496](https://doi.org/10.1086/115496)
- Rastello, S., Carraro, G., & Capuzzo-Dolcetta, R. 2020, *ApJ*, 896, 152, doi: [10.3847/1538-4357/ab910b](https://doi.org/10.3847/1538-4357/ab910b)
- Read, J. I., & Gilmore, G. 2005, *MNRAS*, 356, 107, doi: [10.1111/j.1365-2966.2004.08424.x](https://doi.org/10.1111/j.1365-2966.2004.08424.x)
- Read, J. I., Iorio, G., Agertz, O., & Fraternali, F. 2017, *MNRAS*, 467, 2019, doi: [10.1093/mnras/stx147](https://doi.org/10.1093/mnras/stx147)
- Read, J. I., & Steger, P. 2017, *MNRAS*, 471, 4541, doi: [10.1093/mnras/stx1798](https://doi.org/10.1093/mnras/stx1798)
- Read, J. I., Walker, M. G., & Steger, P. 2018, *MNRAS*, 481, 860, doi: [10.1093/mnras/sty2286](https://doi.org/10.1093/mnras/sty2286)
- Read, J. I., Mamon, G. A., Vasiliev, E., et al. 2021, *MNRAS*, 501, 978, doi: [10.1093/mnras/staa3663](https://doi.org/10.1093/mnras/staa3663)
- Rizzi, L. 2002, PhD thesis, Padova Univ.
- Robitaille, T., & Bressert, E. 2012, APLpy: Astronomical Plotting Library in Python, Astrophysics Source Code Library. <http://ascl.net/1208.017>
- Savino, A., Weisz, D. R., Dolphin, A. E., et al. 2025, *ApJ*, 979, 205, doi: [10.3847/1538-4357/ada24f](https://doi.org/10.3847/1538-4357/ada24f)
- Shapley, H. 1938, *Nature*, 142, 715, doi: [10.1038/142715b0](https://doi.org/10.1038/142715b0)
- Silk, J., & Mamon, G. A. 2012, *Research in Astronomy and Astrophysics*, 12, 917, doi: [10.1088/1674-4527/12/8/004](https://doi.org/10.1088/1674-4527/12/8/004)
- Sohn, S. T., del Pino Molina, A., Besla, G., et al. 2021, Internal Proper Motion Kinematics of Dwarf Spheroidal Galaxies: Constraining the Density and Properties of Dark Matter, HST Proposal. Cycle 29, ID. #16737
- Sohn, S. T., Patel, E., Besla, G., et al. 2017, *ApJ*, 849, 93, doi: [10.3847/1538-4357/aa917b](https://doi.org/10.3847/1538-4357/aa917b)
- Spencer, M. E., Mateo, M., Olszewski, E. W., et al. 2018, *AJ*, 156, 257, doi: [10.3847/1538-3881/aae3e4](https://doi.org/10.3847/1538-3881/aae3e4)
- Springel, V., Wang, J., Vogelsberger, M., et al. 2008, *MNRAS*, 391, 1685, doi: [10.1111/j.1365-2966.2008.14066.x](https://doi.org/10.1111/j.1365-2966.2008.14066.x)
- Strigari, L. E. 2013, *PhR*, 531, 1, doi: [10.1016/j.physrep.2013.05.004](https://doi.org/10.1016/j.physrep.2013.05.004)
- Tchiorniy, K., & Genina, A. 2025, arXiv e-prints, arXiv:2504.18617, doi: [10.48550/arXiv.2504.18617](https://doi.org/10.48550/arXiv.2504.18617)
- Tolstoy, E., Hill, V., & Tosi, M. 2009, *ARA&A*, 47, 371, doi: [10.1146/annurev-astro-082708-101650](https://doi.org/10.1146/annurev-astro-082708-101650)
- Tolstoy, E., Irwin, M. J., Helmi, A., et al. 2004, *ApJL*, 617, L119, doi: [10.1086/427388](https://doi.org/10.1086/427388)
- Tolstoy, E., Skúladóttir, Á., Battaglia, G., et al. 2023, *A&A*, 675, A49, doi: [10.1051/0004-6361/202245717](https://doi.org/10.1051/0004-6361/202245717)
- van der Marel, R. P. 1991, *MNRAS*, 253, 710, doi: [10.1093/mnras/253.4.710](https://doi.org/10.1093/mnras/253.4.710)
- van der Marel, R. P., Alves, D. R., Hardy, E., & Suntzeff, N. B. 2002, *AJ*, 124, 2639, doi: [10.1086/343775](https://doi.org/10.1086/343775)
- van der Marel, R. P., & Anderson, J. 2010, *ApJ*, 710, 1063, doi: [10.1088/0004-637X/710/2/1063](https://doi.org/10.1088/0004-637X/710/2/1063)
- van der Marel, R. P., Anderson, J., Bellini, A., et al. 2023, Internal Dynamics of Milky Way Dwarf Spheroidal Galaxies, JWST Proposal. Cycle 3, ID. #4513
- van der Walt, S., Colbert, S. C., & Varoquaux, G. 2011, *Computing in Science Engineering*, 13, 22
- Van Rossum, G., & Drake, F. L. 2009, *Python 3 Reference Manual* (Scotts Valley, CA: CreateSpace)
- Vasiliev, E. 2019, *MNRAS*, 482, 1525, doi: [10.1093/mnras/sty2672](https://doi.org/10.1093/mnras/sty2672)
- Vitral, E. 2021, *MNRAS*, 504, 1355, doi: [10.1093/mnras/stab947](https://doi.org/10.1093/mnras/stab947)
- Vitral, E., Kremer, K., Libralato, M., Mamon, G. A., & Bellini, A. 2022, *MNRAS*, 514, 806, doi: [10.1093/mnras/stac1337](https://doi.org/10.1093/mnras/stac1337)
- Vitral, E., Libralato, M., Kremer, K., et al. 2023a, *MNRAS*, 522, 5740, doi: [10.1093/mnras/stad1068](https://doi.org/10.1093/mnras/stad1068)

- Vitral, E., Sohn, S. T., Bellini, A., et al. 2023b, Shedding Light on Dark Matter: Internal Proper Motions in Ursa Minor, HST Proposal. Cycle 31, ID. #17434
- Vitral, E., van der Marel, R. P., Sohn, S. T., et al. 2024, ApJ, 970, 1, doi: [10.3847/1538-4357/ad571c](https://doi.org/10.3847/1538-4357/ad571c)
- Walker, M. G., Caldwell, N., Mateo, M., et al. 2023, ApJS, 268, 19, doi: [10.3847/1538-4365/acdd79](https://doi.org/10.3847/1538-4365/acdd79)
- Walker, M. G., Mateo, M., Olszewski, E. W., et al. 2007, ApJS, 171, 389, doi: [10.1086/517886](https://doi.org/10.1086/517886)
- Walker, M. G., & Peñarrubia, J. 2011, ApJ, 742, 20, doi: [10.1088/0004-637X/742/1/20](https://doi.org/10.1088/0004-637X/742/1/20)
- Wang, W., Zhu, L., Jing, Y., et al. 2023, ApJ, 956, 91, doi: [10.3847/1538-4357/acf314](https://doi.org/10.3847/1538-4357/acf314)
- Watkins, L. L., van de Ven, G., den Brok, M., & van den Bosch, R. C. E. 2013, MNRAS, 436, 2598, doi: [10.1093/mnras/stt1756](https://doi.org/10.1093/mnras/stt1756)
- Watkins, L. L., van der Marel, R. P., Bellini, A., & Anderson, J. 2015, ApJ, 803, 29, doi: [10.1088/0004-637X/803/1/29](https://doi.org/10.1088/0004-637X/803/1/29)
- Zhao, H. 1996, MNRAS, 278, 488
- Zhu, L., van de Ven, G., Watkins, L. L., & Posti, L. 2016, MNRAS, 463, 1117, doi: [10.1093/mnras/stw2081](https://doi.org/10.1093/mnras/stw2081)

APPENDIX

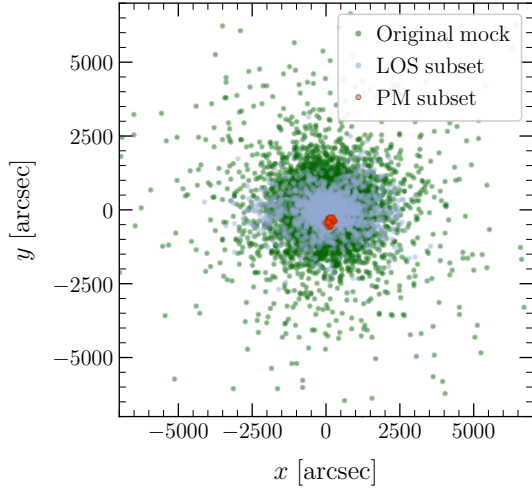


Figure 14. *Sky view of mock data:* The positions of the stars in our mock dataset, with x and y directions aligned to the galaxy’s major and minor axes, are shown at three stages of the mock data construction. The original stars, sampled using the AGAMA software, are depicted in green. Stars associated with line-of-sight velocity measurements are shown in blue, while those with proper motion measurements are in red. This configuration enables us to assess the effect of spatial incompleteness on our final estimates.

A. MOCK DATA RECIPE

In this section, we outline the procedure used to construct realistic mock datasets from the raw output generated by the AGAMA distribution function-based software (Vasiliev 2019). This output provides phase-space information for a given kinematical population, with stars distributed according to a specified input density profile within a given potential. For context, we adopted AGAMA’s *QuasiSpherical* distribution function,³⁹ assuming constant velocity anisotropy. This was set to isotropic in mock test #1 (cf. Section 5.2.1), and matched to the mean anisotropies inferred for Sculptor’s metal-poor and metal-rich populations from figure 1 of Arroyo-Polonio et al. (2025) in mock test #2 (cf. Section 5.2.2). In mock test #1, we also introduced a mild rotational component by flipping the velocity vectors of 20% of the stars⁴⁰ with $L_z < 0$. To ensure that this rotation would produce observable signatures in the plane

of the sky, we adopted an intermediate inclination of $i = 57^\circ.1$, deviating from an edge-on configuration where PM streaming would become undetectable. This setup allowed us to reproduce a scenario broadly consistent with the inclination constraints from Section 4.1.1, while still enabling a meaningful test of our artificial removal of streaming motions in the PM data.

The first step once the AGAMA outcome was ready involved converting the physical quantities of velocities and sky positions into observed, angular-based quantities, assuming a specific distance to the galaxy. We adopted the same distance value used in the priors for our Jeans modeling. Next, we applied local corrections to the PM components of the mock data, following the same procedure outlined in Section 2.3.2 and in Paper I. This correction effectively removed any trace of transverse streaming motions from the mock data.

The next step was to select stars located within the same sky region as the real data for each subset (i.e., the LOS and PM subsets). This was accomplished by first identifying the stars within a convex hull defined by the spatial boundaries of each observed dataset. We then randomly selected the same number of stars from these regions as were present in the observations, aiming to assess the influence of spatial incompleteness on our estimates. Figure 14 illustrates the spatial distribution of the stars in each of the three components: the original mock data sampled by AGAMA (shown in green), the selected LOS subset (in blue), and the PM subset (in red).

The final step was to assign realistic uncertainties to both the v_{LOS} and PM quantities. To do so, we first derived error distributions independently for each set: for the LOS velocities, we sampled from the 1D distribution of observed $\epsilon_{v_{\text{LOS}}}$, while for the PMs, we drew from the correlated 2D distribution of observed $\epsilon_{\mu_{\alpha,*}}$ vs. $\epsilon_{\mu_{\delta}}$, which incorporated both the nominal uncertainties and those introduced by the local systematic corrections. From these distributions, we added zero-centered Gaussian random variables, with standard deviations corresponding to the computed errors, to the respective v_{LOS} and PM values, thus completing the mock data construction.

B. ONLINE MATERIAL

³⁹ Details of this module are available in the software documentation: <https://github.com/GalacticDynamics-Oxford/Agama>.

⁴⁰ This choice reflects our findings from Section 2.2.2, where a similarly low rotation amplitude was observed.

Table 3. Proper motion catalog.

α	δ	$\mu_{\alpha,*}$	$\epsilon_{\mu_{\alpha,*}}$	μ_{δ}	$\epsilon_{\mu_{\delta}}$	F775W	F606W	ID
[$^{\circ}$]	[$^{\circ}$]	[mas yr $^{-1}$]	[mas yr $^{-1}$]	[mas yr $^{-1}$]	[mas yr $^{-1}$]	[dex]	[dex]	
(1)	(2)	(3)	(4)	(5)	(6)	(7)	(8)	(9)
14.98182	−33.84174	0.0259	0.0189	−0.0052	0.0196	−11.3723	−11.4352	1
14.99856	−33.83554	0.0238	0.0225	−0.0191	0.0227	−11.5420	−11.0647	2
15.00169	−33.84224	0.0128	0.0189	0.0222	0.0155	−11.3253	−10.8545	3
\vdots								

NOTES – Columns are **(1)** Right ascension, in degrees; **(2)** Declination, in degrees; **(3)** Proper motion in right ascension, $(d\alpha/dt) \cos \delta$, in mas yr $^{-1}$; **(4)** Uncertainty in $\mu_{\alpha,*}$, in mas yr $^{-1}$; **(5)** Proper motion in declination, $(d\delta/dt)$, in mas yr $^{-1}$; **(6)** Uncertainty in μ_{δ} , in mas yr $^{-1}$; **(7)** Instrumental F775W magnitude, in unities of $-2.5 \log c$, where c is the electron count per exposure for a source in this filter; **(8)** Instrumental F606W magnitude, in unities of $-2.5 \log c$, where c is the electron count per exposure for a source in this filter; **(9)** Internal ID of star. The proper motions are not absolute on the sky, but relative to motion of Sculptor, and with mean motion (i.e. first order moments) signatures removed by construction, as described in Section 2.3.2. Hence, the proper motions are centered at $(\mu_{\alpha,*}, \mu_{\delta}) = (0, 0)$. A full readable version of this table will be available as online material.

Table 4. Line-of-sight velocity catalog.

α	δ	v_{LOS}	$\epsilon_{v_{\text{LOS}}}$	N_{spec}	ID _{Tolstoy}	ID _{Walker}
[$^{\circ}$]	[$^{\circ}$]	[km s $^{-1}$]	[km s $^{-1}$]			
(1)	(2)	(3)	(4)	(5)	(6)	(7)
13.66484	−33.52300	120.5981	0.4182	2	scl011_09_	–
13.87452	−33.76831	119.8343	0.9640	3	scl_11_040	–
13.93013	−34.02570	123.5945	0.4500	1	scl020-12_	–
\vdots						

NOTES – Columns are **(1)** Right ascension, in degrees; **(2)** Declination, in degrees; **(3)** Line-of-sight velocity, in km s $^{-1}$; **(4)** Uncertainty in line-of-sight velocity, in km s $^{-1}$; **(5)** Number of spectra used to construct this measurement (for matches between two catalogs, this is the sum of spectra used in each entry); **(6)** Star ID in Tolstoy et al. (2023) catalog; **(7)** Star ID in Walker et al. (2023) catalog.

In this section, we briefly describe the kinematic datasets used in this study, which are provided as online material. These include a proper-motion table (Table 3) derived from the *HST* observations presented here, and a line-of-sight velocity table (Table 4) assembled by cross-matching the original catalogs of Tolstoy et al. (2023) and Walker et al. (2023). For further details on how the data was assembled, see Sections 2.2 and 2.3.